Journal of Computational Physics **163,** 83–117 (2000)
doi:10.1006/jcph.2000.6556, available online at http://www.idealibrary.com on IDEAL®

Active Control and Drag Optimization for Flow Past a Circular Cylinder

I. Oscillatory Cylinder Rotation[1]

J.-W. He,* R. Glowinski,* R. Metcalfe,† A. Nordlander,† and J. Periaux‡

*Department of Mathematics and †Department of Mechanical Engineering, University of Houston, Houston, Texas 77204; and ‡Dassault Aviation, 78 quai Marcel Dassault, 92214 Saint Cloud, France
E-mail: jiwenhe@math.uh.edu, roland@math.uh.edu, metcalfe@uh.edu, andersn@math.uh.edu, periaux@menusin.inria.fr

Received September 16, 1999; revised April 14, 2000

DEDICATED TO D. D. JOSEPH AND J. L. LIONS ON THE OCCASION OF THEIR 70TH BIRTHDAYS AND FOR THEIR OUTSTANDING CONTRIBUTIONS TO THE NAVIER–STOKES EQUATIONS AND TO FLOW CONTROL

The main objective of this article is to investigate computational methods for the active control and drag optimization of incompressible viscous flow past cylinders, using the two-dimensional Navier–Stokes equations as the flow model. The computational methodology relies on the following ingredients: space discretization of the Navier–Stokes equations by finite element approximations, time discretization by a second-order-accurate two-step implicit/explicit finite difference scheme, calculation of the cost function gradient by the adjoint equation approach, and minimization of the cost function by a quasi-Newton method à la BFGS. The above methods have been applied to boundary control by rotation of the flow around a circular cylinder and show 30 to 60% drag reduction, compared to the fixed cylinder configuration, for Reynolds numbers in the range from 200 to 1000.

Key Words: active flow control; Navier–Stokes equations; optimal control; adjoint equations; BFGS algorithms; finite difference methods; finite element methods.

CONTENTS

[1] Supported in part by the Higher Education Texas Coordinating Board, by the National Science Foundation, and by Dassault Aviation.

0021-9991/00 $35.00

4. *Full discretization of the control problem.*
5. *Gradient calculation.*
6. *A BFGS algorithm for the discrete control problem.*
7. *Validation of the flow simulator.*
8. *Active control by rotation: Numerical results.*
9. *Conclusions.*

1. INTRODUCTION

Engineers have not waited for mathematicians to successfully address flow control problems (see, e.g., Refs. [7, 19] for a review on flow control from the engineering point of view); indeed, Prandtl as early as 1915 was concerned with flow control and was designing ingenious systems to suppress or delay boundary layer separation [30]. The past decade has seen an explosive growth of investigations and publications of a mathematical nature concerning various aspects of the control of viscous flow, good examples being provided in [18, 34]. Actually these two volumes also contain some articles related to the computational aspect of the optimal control of viscous flow, but usually, the geometries are fairly simple and the Reynolds numbers fairly low. It is interesting to observe that the *Journal of Computational Physics* has published recently articles on the above topics (see Refs. [10, 23, 25]); however, in those articles, once again, the geometry is simple and/or the Reynolds number is low.

The main goal of this article is to investigate computational methods for the active control and drag optimization of incompressible viscous flow past cylinders, using the two-dimensional Navier–Stokes equations as the flow model. The computational methodology relies on the following ingredients: Space discretization of the Navier–Stokes equations by finite element approximations, time discretization by a second-order-accurate two-step implicit/explicit finite difference scheme, calculation of the cost function gradient by the adjoint equation approach, and minimization of the cost function by a quasi-Newton method à la BFGS. Motivated in part by the experimental work of Tokumaru and Dimotakis [36], the above methods have been applied to boundary control by rotation of the flow around a circular cylinder and show 30 to 60% drag reduction, compared to the fixed cylinder configuration, for Reynolds numbers in the range of 200 to 1000.

From a methodological point of view, some of the methods used here are clearly related to those employed by our former collaborator M. Berggren in [4] for boundary control by blowing and suction of incompressible viscous flow in bounded cavities. In fact, the method described in the present article has been extended in [8] to the drag reduction of viscous flow around a cylinder by blowing and suction, leading to further "net" drag reduction compared to the control by rotation; an article to appear in the open literature is in preparation.

The organization of the remainder of the paper is as follows: In Section 2 we formulate the flow control problem and address its time discretization in Section 3. The important problem of the space discretization by the finite element method is discussed in Section 4; special attention is given there to velocity spaces, which are discretely divergence-free in order to reduce the number of algebraic constraints in the control problem. The full discretization of the control problem is addressed in Section 5. Since we intend to use solution methods based on a quasi-Newton algorithm à la BFGS (see Section 6), attention is focused in Section 5 on the derivation of the gradient of the fully discrete cost function via the classical adjoint

equation method. The flow simulator (actually a Navier–Stokes equations solver) is further discussed in Section 7, where it is validated on well-documented flow-around-cylinder test problems for various values of the Reynolds number. Finally, the results of various numerical experiments for flow control past a cylinder are discussed in Section 8; they definitely show that a substantial drag reduction can be obtained by an appropriate rotation of the cylinder.

2. FORMULATION OF THE FLOW CONTROL PROBLEM

2.1. *Fluid Flow Formulation*

Let Ω be a region of $\mathbb{R}^d$ ($d = 2, 3$ in practice); we denote by Γ the boundary $\partial\Omega$ of Ω. We assume that Ω is filled with a Newtonian incompressible viscous fluid of *density* ρ and *viscosity* μ; we assume that the temperature is constant. Under these circumstances the flow of such a fluid is modeled by the following system of Navier–Stokes equations:

$$\rho\,[\partial_t \mathbf{y} + (\mathbf{y}\cdot\nabla)\mathbf{y}] = \nabla\cdot\sigma + \rho\mathbf{f} \qquad \text{in } \Omega\times(0,T), \tag{1}$$

$$\nabla\cdot\mathbf{y} = 0 \qquad \text{in } \Omega\times(0,T) \text{ (incompressibility condition)}. \tag{2}$$

In (1), (2), $\mathbf{y} = \{y_i\}_{i=1}^d$ denotes the *velocity* field, π the *pressure*, $\mathbf{f}$ a density of external forces per mass unit, and $\sigma\,(=\sigma(\mathbf{y},\pi))$ the stress tensor, defined by

$$\sigma = 2\mu\mathbf{D}(\mathbf{y}) - \pi\mathbf{I},$$

with the *rate of deformation tensor* $\mathbf{D}(\mathbf{y})$ defined by

$$\mathbf{D}(\mathbf{y}) = \frac{1}{2}(\nabla\mathbf{y} + \nabla\mathbf{y}^t).$$

We also have

$$\partial_t = \frac{\partial}{\partial t}, \qquad \nabla^2 = \sum_{i=1}^d \frac{\partial^2}{\partial x_i^2}, \qquad \nabla\cdot\mathbf{y} = \sum_{i=1}^d \frac{\partial y_i}{\partial x_i}, \qquad (\mathbf{y}\cdot\nabla)\mathbf{z} = \left\{\sum_{j=1}^d y_j\frac{\partial z_i}{\partial x_j}\right\}_{i=1}^d.$$

In the above equations $(0, T)$ is the *time interval* during which the flow is considered.

Equations (1) and (2) must be completed by further conditions, such as the *initial condition*

$$\mathbf{y}(0) = \mathbf{y}_0 \qquad (\text{with} \nabla\cdot\mathbf{y}_0 = 0) \tag{3}$$

and boundary conditions. Let us consider the typical situation, of interest to us, described in Fig. 1, corresponding to an external flow around a cylinder of cross-section B; we assume that the classical two-dimensional reduction holds.

In fact, $\Gamma_u\cup\Gamma_d\cup\Gamma_N\cup\Gamma_S$ is an *artificial* boundary, which must be taken sufficiently far from B so that the corresponding flow is a good approximation of the unbounded external flow around B. Typical boundary conditions are

$$\mathbf{y} = \mathbf{y}_\infty \qquad \text{on } (\Gamma_u\cup\Gamma_N\cup\Gamma_S)\times(0,T), \tag{4}$$

$$\sigma\,\mathbf{n} = \mathbf{0} \qquad \text{on } \Gamma_d\times(0,T) \text{ (downstream boundary condition)}, \tag{5}$$

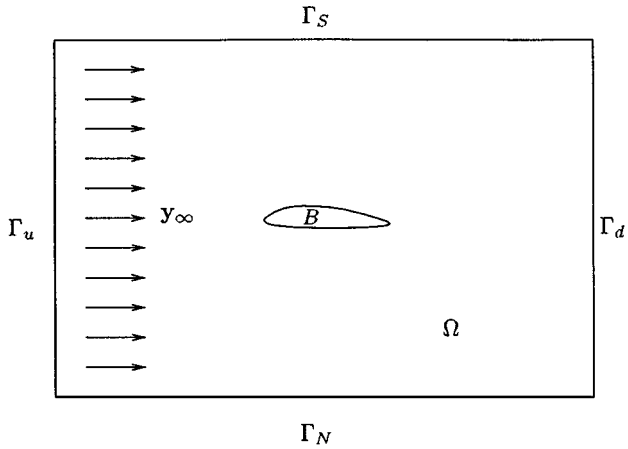

FIG. 1. External flow around a cylinder of cross-section B.

with $\mathbf{n}$ the *unit vector* of the outward normal on Γ. We are intentionally vague concerning the boundary conditions on ∂B, since they will be part of the control process. Let us conclude this paragraph by recalling that the *Reynolds number* Re is classically defined by

$$\mathrm{Re} = \rho U L/\mu, \tag{6}$$

with U a *characteristic velocity* ($|\mathbf{y}_\infty|$, here) and L a *characteristic* length (the thickness of B, for example).

Our goal in this article is to prescribe on ∂B boundary conditions of the *Dirichlet type* (i.e., velocity imposed on ∂B) so that some flow-related performance criterion (the cost function) will be minimized under reasonable constraints on the control variables.

2.2. *Formulation of the Control Problem*

The flow control problem to be discussed in this article consists of minimizing a *drag*-related cost function via controls acting on ∂B; this problem can be formulated (using classical control formalism) as

$$\begin{aligned} &\mathbf{u} \in \mathcal{U}, \\ &J(\mathbf{u}) \le J(\mathbf{v}), \qquad \forall \mathbf{v} \in \mathcal{U}, \end{aligned} \tag{7}$$

where, in (7), the *control space* $\mathcal{U}$ is a vector space of vector-valued functions $\mathbf{v}$ defined on $\partial B \times (0, T)$ and satisfying

$$\int_{\partial B} \mathbf{v}(t) \cdot \mathbf{n}\, ds = 0 \qquad \text{for } t \in (0, T), \tag{8}$$

and where the *cost function* J is defined by

$$J(\mathbf{v}) = \frac{\epsilon}{2}\left(\int_0^T \|\mathbf{v}(t)\|_\alpha^2\, dt + \int_0^T \int_{\partial B} |\partial_t \mathbf{v}(x,t)|^2\, ds\, dt \right) + \int_0^T P_{\mathrm{d}}(t)\, dt, \tag{9}$$

with $\epsilon (\ge 0)$ a *regularization* parameter.

In (8), (9), we have used the following notation:

- $\varphi(t)$ for the function $x \to \varphi(x, t)$.
- ds for the surface measure on ∂B.
- $\|\mathbf{v}\|_\alpha$ for a norm of $\mathbf{v}$ defined on ∂B, involving space derivatives of order α, with α possibly noninteger (readers afraid of these mathematical complications do not have to worry, since in this article we shall consider boundary controls that are functions of t only).
- $P_{\mathrm{d}}(t)$ is the power needed to overcome, at time t, the drag exerted on B in the direction opposite to that of the motion; $P_{\mathrm{d}}(t)$ is defined by

$$P_{\mathrm{d}}(t) = \int_{\partial B} \sigma\, \mathbf{n} \cdot (\mathbf{v} - \mathbf{y}_\infty)\, ds. \tag{10}$$

- Finally, $\mathbf{y}$ is the solution to the following Navier–Stokes system:

$$\rho\,[\partial_t \mathbf{y} + (\mathbf{y} \cdot \nabla)\mathbf{y}] = \nabla \cdot \sigma + \rho \mathbf{f} \qquad \text{in } \Omega \times (0, T), \tag{11}$$

$$\nabla \cdot \mathbf{y} = 0 \qquad \text{in } \Omega \times (0, T), \tag{12}$$

$$\mathbf{y}(0) = \mathbf{y}_0 \qquad (\text{with } \nabla \cdot \mathbf{y}_0 = 0), \tag{13}$$

$$\sigma \mathbf{n} = \mathbf{0} \qquad \text{on } \Gamma_{\mathrm{d}} \times (0, T), \tag{14}$$

$$\mathbf{y} = \mathbf{y}_\infty \qquad \text{on } (\Gamma_{\mathrm{u}} \cup \Gamma_{\mathrm{N}} \cup \Gamma_{\mathrm{S}}) \times (0, T), \tag{15}$$

$$\mathbf{y} = \mathbf{v} \qquad \text{on } \partial B \times (0, T). \tag{16}$$

Remark 2.1. The flux condition (8) is not essential and can be easily relaxed if, for example, the downstream boundary conditions are of Neumann type (like those in (14)).

Remark 2.2. The Navier–Stokes equation (11) can also be written

$$\rho\,[\partial_t \mathbf{y} + (\mathbf{y} \cdot \nabla)\mathbf{y}] - \mu \nabla^2 \mathbf{y} + \nabla \pi = \rho \mathbf{f} \qquad \text{in } \Omega \times (0, T);$$

however, form (11) is better suited to the drag reduction problem (7), since, as (10), it involves the stress tensor σ.

Remark 2.3. In the particular case of incompressible viscous flow we have

$$\int_0^T P_{\mathrm{d}}(t)\, dt = \int_0^T E_{\mathrm{d}}(t)\, dt + (K(T) - K(0)) + \int_0^T P_{\mathrm{c}}(t)\, dt + \int_0^T P_\infty(t)\, dt - \int_0^T P_{\mathrm{f}}(t)\, dt, \tag{17}$$

where, in (17),

- $E_{\mathrm{d}}(t) = 2\mu \int_\Omega |\mathbf{D}(\mathbf{y} - \mathbf{y}_\infty)|^2\, dx$ is the *viscous dissipation energy*,
- $K(t) = \frac{\rho}{2} \int_\Omega |\mathbf{y}(t) - \mathbf{y}_\infty|^2\, dx$ is a *kinetic energy*,
- $P_{\mathrm{c}}(t) = \frac{\rho}{2} \int_{\partial B} |\mathbf{v} - \mathbf{y}_\infty|^2 \mathbf{v} \cdot \mathbf{n}\, ds$ is a *control related power*,
- $P_\infty(t) = \frac{\rho}{2} \int_{\Gamma_\infty^{\mathrm{d}}} |\mathbf{y} - \mathbf{y}_\infty|^2 \mathbf{y} \cdot \mathbf{n}\, ds$ is a *downstream boundary related power*,
- $P_{\mathrm{f}}(t) = \rho \int_\Omega \mathbf{f}(t) \cdot (\mathbf{y}(t) - \mathbf{y}_\infty)\, dx$ is the *external forcing power*.

Some observations are in order, such as:

1. If Γ_d "goes to infinity" in the Ox_1 direction, then $\mathbf{y} \to \mathbf{y}_\infty$, which implies in turn that $P_\infty \to 0$.
2. Whenever the control is absent, i.e., $\mathbf{v} = \mathbf{0}$, we have $P_c(t) = 0$.

We can summarize relation (17) by noting that "the drag work is equal to the energy dissipated by viscosity + the kinetic energy variation between 0 and T + the control associated work + the downstream boundary associated work − the external forcing work." The above observation has the following consequence: instead of minimizing $J(\cdot)$ defined by (9) we can minimize the cost function $J(\cdot)$ defined by

$$J(\mathbf{v}) = \frac{\epsilon}{2}\left(\int_0^T \|\mathbf{v}(t)\|_\alpha^2\, dt + \int_0^T \int_{\partial B} |\partial_t \mathbf{v}(x,t)|^2\, ds\, dt\right) + \int_0^T E_d(t)\, dt + (K(T) - K(0)) + \int_0^T P_c(t)\, dt + \int_0^T P_\infty(t)\, dt - \int_0^T P_f(t)\, dt;$$

this function is simpler than the one defined by (9) since it does not involve boundary integrals of stress-tensor-related quantities. However, we kept working with the cost function defined by (9) using an appropriate variational formulation of the discrete Navier–Stokes equations (see Section 4.3 for details); we can easily compute an accurate approximation of the drag (actually second order accurate as shown in [35], where a similar approach has been used for computing the drag coefficients of a sphere).

In order to apply *quasi-Newton-type methods* à la BFGS to the solution of the control problem (7), it is instrumental to know how to compute the gradient of the cost function $J_h^{\Delta t}(\cdot)$, obtained from the full space-time discretization of the control problem (7), since we shall solve the discrete variant of problem (7) via the (necessary) *optimality condition*

$$\nabla J_h^{\Delta t}\left(\mathbf{u}_h^{\Delta t}\right) = \mathbf{0},$$

where $\mathbf{u}_h^{\Delta t}$ is a solution of the fully discrete control problem. The calculation of $\nabla J_h^{\Delta t}$ will be discussed in Section 5.

3. TIME DISCRETIZATION OF THE CONTROL PROBLEM

3.1. *Generalities*

In order to facilitate the task of the reader unfamiliar with control methodology (not to say philosophy) we are going to discuss first the *time discretization* issue. The space and consequently full space/time discretization issues will be addressed in Section 4. This approach of fractioning the computational difficulties has the definite advantage that some practitioners will be able to use the material in this article for other types of space approximations than the finite element ones discussed in Section 4 (one may prefer spectral methods, for example).

3.2. *Formulation of the Time Discrete Control Problem*

We define first a time discretization step Δt by $\Delta t = T/N$, with N a (large) positive integer. Concentrating on problem (7), we approximate it by

$$\begin{aligned} &\mathbf{u}^{\Delta t} \in \mathcal{U}^{\Delta t}, \\ &J^{\Delta t}(\mathbf{u}^{\Delta t}) \le J^{\Delta t}(\mathbf{v}), \qquad \forall \mathbf{v} \in \mathcal{U}^{\Delta t}, \end{aligned} \tag{18}$$

with

$$\mathcal{U}^{\Delta t} = \mathbf{\Lambda}^N, \tag{19}$$

$$\mathbf{\Lambda} = \left\{ \boldsymbol{\lambda} \mid \boldsymbol{\lambda} \in (H^\alpha(\partial\Omega))^d, \int_{\partial B} \boldsymbol{\lambda} \cdot \mathbf{n}\, ds = 0 \right\}, \tag{20}$$

and

$$J^{\Delta t}(\mathbf{v}) = \frac{\epsilon}{2}\,\Delta t \left(\sum_{n=1}^{N} \|\mathbf{v}^n\|_\alpha^2 + \sum_{n=2}^{N} \left\| \frac{\mathbf{v}^n - \mathbf{v}^{n-1}}{\Delta t} \right\|_0^2 \right) + \Delta t \sum_{n=1}^{N} P_{\mathrm{d}}^n, \tag{21}$$

where, in (21), P_{d}^n is the discrete drag power defined (with obvious notation) by

$$P_{\mathrm{d}}^n = \int_{\partial B} \sigma(\mathbf{y}^n, \pi^n)\, \mathbf{n} \cdot (\mathbf{v}^n - \mathbf{y}_\infty)\, ds$$

with $\{(\mathbf{y}^n, \pi^n)\}_{n=1}^N$ obtained from $\mathbf{v}$ via the solution of the following semi-discrete Navier–Stokes equations:

$$\mathbf{y}^0 = \mathbf{y}_0, \tag{22}$$

$$\rho\left(\frac{\mathbf{y}^1 - \mathbf{y}^0}{\Delta t} + (\mathbf{y}^0 \cdot \nabla)\mathbf{y}^0 \right) = \nabla \cdot \sigma\left(\frac{2}{3}\mathbf{y}^1 + \frac{1}{3}\mathbf{y}^0, \pi^1 \right) + \rho \mathbf{f}^1 \qquad \text{in } \Omega, \tag{23}$$

$$\nabla \cdot \mathbf{y}^1 = 0 \qquad \text{in } \Omega, \tag{24}$$

$$\sigma\left(\frac{2}{3}\mathbf{y}^1 + \frac{1}{3}\mathbf{y}^0, \pi^1 \right)\mathbf{n} = \mathbf{0} \qquad \text{on } \Gamma_{\mathrm{d}}, \tag{25}$$

$$\mathbf{y}^1 = \mathbf{y}_\infty \qquad \text{on } \Gamma_{\mathrm{u}} \cup \Gamma_{\mathrm{N}} \cup \Gamma_{\mathrm{S}}, \tag{26}$$

$$\mathbf{y}^1 = \mathbf{v}^1 \qquad \text{on } \partial B, \tag{27}$$

and for $n = 2, \ldots, N$

$$\rho\left(\frac{(3/2)\mathbf{y}^n - 2\mathbf{y}^{n-1} + (1/2)\mathbf{y}^{n-2}}{\Delta t} + ((2\mathbf{y}^{n-1} - \mathbf{y}^{n-2}) \cdot \nabla)(2\mathbf{y}^{n-1} - \mathbf{y}^{n-2}) \right)$$
$$= \nabla \cdot \sigma(\mathbf{y}^n, \pi^n) + \rho \mathbf{f}^n \qquad \text{in } \Omega, \tag{28}$$

$$\nabla \cdot \mathbf{y}^n = 0 \qquad \text{in } \Omega, \tag{29}$$

$$\sigma(\mathbf{y}^n, \pi^n)\, \mathbf{n} = \mathbf{0} \qquad \text{on } \Gamma_{\mathrm{d}}, \tag{30}$$

$$\mathbf{y}^n = \mathbf{y}_\infty \qquad \text{on } \Gamma_{\mathrm{u}} \cup \Gamma_{\mathrm{N}} \cup \Gamma_{\mathrm{S}}, \tag{31}$$

$$\mathbf{y}^n = \mathbf{v}^n \qquad \text{on } \partial B. \tag{32}$$

The above scheme is a semi-implicit, second-order-accurate two-step scheme.

Anticipating the finite element approximation to take place in the following section, we can rewrite (23)–(32) in *variational form*. We obtain thus

$$\rho \int_\Omega \frac{\mathbf{y}^1 - \mathbf{y}^0}{\Delta t} \cdot \mathbf{z}\, dx + 2\mu \int_\Omega \mathbf{D}\left(\frac{2}{3}\mathbf{y}^1 + \frac{1}{3}\mathbf{y}^0 \right) : \mathbf{D}(\mathbf{z})\, dx$$
$$+ \rho \int_\Omega (\mathbf{y}^0 \cdot \nabla)\mathbf{y}^0 \cdot \mathbf{z}\, dx - \int_\Omega \pi^1 \nabla \cdot \mathbf{z}\, dx$$
$$= \rho \int_\Omega \mathbf{f}^1 \cdot \mathbf{z}\, dx, \qquad \forall \mathbf{z} \in \mathbf{V}_0, \tag{33}$$

$$\int_\Omega \nabla \cdot \mathbf{y}^1 q \, dx = 0, \qquad \forall q \in L^2(\Omega), \tag{34}$$

$$\mathbf{y}^1 = \mathbf{y}_\infty \qquad \text{on } \Gamma_u \cup \Gamma_N \cup \Gamma_S, \tag{35}$$

$$\mathbf{y}^1 = \mathbf{v}^1 \qquad \text{on } \partial B; \tag{36}$$

and for $n = 2, \ldots, N$

$$\begin{aligned} \rho \int_\Omega \frac{(3/2)\mathbf{y}^n - 2\mathbf{y}^{n-1} + (1/2)\mathbf{y}^{n-2}}{\Delta t} \cdot \mathbf{z} \, dx + 2\mu \int_\Omega \mathbf{D}(\mathbf{y}^n) : \mathbf{D}(\mathbf{z}) \, dx \\ + \rho \int_\Omega ((2\mathbf{y}^{n-1} - \mathbf{y}^{n-2}) \cdot \nabla)(2\mathbf{y}^{n-1} - \mathbf{y}^{n-2}) \cdot \mathbf{z} \, dx - \int_\Omega \pi^n \nabla \cdot \mathbf{z} \, dx \\ = \rho \int_\Omega \mathbf{f}^n \cdot \mathbf{z} \, dx, \qquad \forall \mathbf{z} \in \mathbf{V}_0, \end{aligned} \tag{37}$$

$$\int_\Omega \nabla \cdot \mathbf{y}^n q \, dx = 0, \qquad \forall q \in L^2(\Omega), \tag{38}$$

$$\mathbf{y}^n = \mathbf{y}_\infty \qquad \text{on } \Gamma_u \cup \Gamma_N \cup \Gamma_S, \tag{39}$$

$$\mathbf{y}^n = \mathbf{v}^n \qquad \text{on } \partial B. \tag{40}$$

In (33), (37), we have used the notation

$$\mathbf{T} : \mathbf{S} = \sum_{i=1}^{d} \sum_{j=1}^{d} t_{ij} s_{ij}$$

to denote the scalar product in $\mathbb{R}^{d^2}$ of the two tensors $\mathbf{T} = \{t_{ij}\}_{i,j=1}^d$ and $\mathbf{S} = \{s_{ij}\}_{i,j=1}^d$, and the space $\mathbf{V}_0$ is defined by

$$\mathbf{V}_0 = \{ \mathbf{z} \,|\, \mathbf{z} \in (H^1(\Omega))^d, \ \mathbf{z} = \mathbf{0} \qquad \text{on } \Gamma_u \cup \Gamma_N \cup \Gamma_S \cup \partial B \}. \tag{41}$$

3.3 *Comments on the Time Discretization of the Control Problem (7)*

Since the time discretization step used in Section 3.2 is a two-step one, a *starting procedure* is required; the one we have used, namely, (23)–(27), leads to a generalized Stokes problem to obtain $\{\mathbf{y}^1, \pi^1\}$ which has the same coefficients as the ones used to obtain $\{\mathbf{y}^n, \pi^n\}$ from $\mathbf{v}^n$ and $\mathbf{y}^{n-1}$, $\mathbf{y}^{n-2}$. As we shall see later on in this article, scheme (22)–(32), albeit partly explicit, has shown very good robustness properties when applied to the solution of drag reduction problems.

4. FULL DISCRETIZATION OF THE CONTROL PROBLEM

4.1. *Synopsis*

In order to *spatially discretize* the control problem (7), we are going to use a *finite element* approximation, since this kind of approximation is well suited to handling complicated boundaries and boundary conditions. The discretization to be used combines a continuous

piecewise Q_2-approximation for the velocity and a discontinuous P_1-approximation for the pressure (with P_1 (resp., Q_2) the space of the polynomials in x_1, x_2 of degree ≤ 1 (resp., of degree ≤ 2 with respect to each variable)). This approximation satisfies a *discrete inf–sup condition*, implying that the discrete problems are well-posed and the approximation is convergent (see, e.g., [6, 11, 17, 29] for the finite element approximation of the Navier–Stokes equations).

4.2. *Discrete Flow Model*

In order to fully discretize the semi-discrete model (22)–(32) we are going to mimic its equivalent formulation. Doing so, we obtain

$$\mathbf{y}_h^0 = \mathbf{y}_{0h} \text{ (a convenient approximation of } \mathbf{y}_0); \tag{42}$$

and

$$\begin{aligned} &\rho \int_{\Omega_h} \frac{\mathbf{y}_h^1 - \mathbf{y}_h^0}{\Delta t} \cdot \mathbf{z}\, dx + 2\mu \int_{\Omega_h} \mathbf{D}\left(\frac{2}{3}\mathbf{y}_h^1 + \frac{1}{3}\mathbf{y}_h^0\right) : \mathbf{D}(\mathbf{z})\, dx \\ &\quad + \rho \int_{\Omega_h} \left(\mathbf{y}_h^0 \cdot \nabla\right)\mathbf{y}_h^0 \cdot \mathbf{z}\, dx - \int_{\Omega_h} \pi_h^1 \nabla \cdot \mathbf{z}\, dx \\ &= \rho \int_{\Omega_h} \mathbf{f}^1 \cdot \mathbf{z}\, dx, \qquad \forall \mathbf{z} \in \mathbf{V}_{0h}, \end{aligned} \tag{43}$$

$$\int_{\Omega_h} \nabla \cdot \mathbf{y}_h^1 q\, dx = 0, \qquad \forall q \in \mathbf{P}_h, \tag{44}$$

$$\mathbf{y}_h^1 = \mathbf{y}_\infty \qquad \text{on } \Gamma_{\mathrm{u},h} \cup \Gamma_{\mathrm{N},h} \cup \Gamma_{\mathrm{S},h}, \tag{45}$$

$$\mathbf{y}_h^1 = \mathbf{v}^1 \qquad \text{on } \partial B_h; \tag{46}$$

then for $n = 2, \ldots, N$,

$$\begin{aligned} &\rho \int_{\Omega_h} \frac{(3/2)\mathbf{y}_h^n - 2\mathbf{y}_h^{n-1} + (1/2)\mathbf{y}_h^{n-2}}{\Delta t} \cdot \mathbf{z}\, dx + 2\mu \int_{\Omega_h} \mathbf{D}\left(\mathbf{y}_h^n\right) : \mathbf{D}(\mathbf{z})\, dx \\ &\quad + \rho \int_{\Omega_h} \left(\left(2\mathbf{y}_h^{n-1} - \mathbf{y}_h^{n-2}\right) \cdot \nabla\right)\left(2\mathbf{y}_h^{n-1} - \mathbf{y}_h^{n-2}\right) \cdot \mathbf{z}\, dx - \int_{\Omega_h} \pi_h^n \nabla \cdot \mathbf{z}\, dx \\ &= \rho \int_{\Omega_h} \mathbf{f}^n \cdot \mathbf{z}\, dx, \qquad \forall \mathbf{z} \in \mathbf{V}_{0h}, \end{aligned} \tag{47}$$

$$\int_{\Omega_h} \nabla \cdot \mathbf{y}_h^n q\, dx = 0, \qquad \forall q \in \mathbf{P}_h, \tag{48}$$

$$\mathbf{y}_h^n = \mathbf{y}_\infty \qquad \text{on } \Gamma_{\mathrm{u},h} \cup \Gamma_{\mathrm{N},h} \cup \Gamma_{\mathrm{S},h}, \tag{49}$$

$$\mathbf{y}_h^n = \mathbf{v}^n \qquad \text{on } \partial B_h. \tag{50}$$

In formulation (42)–(50) we require

$$\mathbf{y}_h^n \in \mathbf{V}_h, \qquad \forall n = 0, 1, \ldots, N, \tag{51}$$

$$\pi_h^n \in \mathbf{P}_h, \qquad \forall n = 1, \ldots, N. \tag{52}$$

The spaces $\mathbf{V}_h$ and $\mathbf{P}_h$ are defined as

$$\mathbf{V}_h = \{\mathbf{z} \mid \mathbf{z} \in (C^0(\bar{\Omega}))^2,\ \mathbf{z}|_K \in Q_{2K}^2,\ \forall K \in \mathcal{Q}_h\}, \tag{53}$$

$$\mathbf{P}_h = \{q \mid q \in L^2(\Omega_h),\ q|_K \in P_1,\ \forall K \in \mathcal{Q}_h\}, \tag{54}$$

where $\mathcal{Q}_h$ is a "*quadrangulation*" of Ω_h (Ω_h: finite element approximation of Ω) and

$$Q_{2K} = \{\varphi \mid \varphi \circ F_K \in Q_2\}, \tag{55}$$

with F_K a well-chosen one-to-one mapping from $[0,1]^2$ into K, such that $F_K \in Q_2^2$. We also need to introduce the following subspace $\mathbf{V}_{0h}$ of $\mathbf{V}_h$:

$$\mathbf{V}_{0h} = \{\mathbf{z} \mid \mathbf{z} \in \mathbf{V}_h,\ \mathbf{z} = \mathbf{0} \qquad \text{on } \Gamma_{\mathrm{u},h} \cup \Gamma_{\mathrm{N},h} \cup \Gamma_{\mathrm{S},h} \cup \partial B_h\}. \tag{56}$$

Let us introduce now the following subspaces of $\mathbf{V}_h$ and $\mathbf{V}_{0h}$:

$$\mathbf{W}_h = \left\{\mathbf{z} \mid \mathbf{z} \in \mathbf{V}_h,\ \int_K q \nabla \cdot \mathbf{z}\, dx = 0, \forall q \in P_1,\ \forall K \in \mathcal{Q}_h\right\}, \tag{57}$$

$$\mathbf{W}_{0h} = \mathbf{W}_h \cap \mathbf{V}_{0h}. \tag{58}$$

A formulation equivalent to (42)–(50) is provided then by

$$\mathbf{y}_h^0 = \mathbf{y}_{0h} \qquad \text{in } \mathbf{W}_h \tag{59}$$

and

$$\rho \int_{\Omega_h} \frac{\mathbf{y}_h^1 - \mathbf{y}_h^0}{\Delta t} \cdot \mathbf{z}\, dx + 2\mu \int_{\Omega_h} \mathbf{D}\left(\frac{2}{3}\mathbf{y}_h^1 + \frac{1}{3}\mathbf{y}_h^0\right) : \mathbf{D}(\mathbf{z})\, dx + \rho \int_{\Omega_h} (\mathbf{y}_h^0 \cdot \nabla)\mathbf{y}_h^0 \cdot \mathbf{z}\, dx$$
$$= \rho \int_{\Omega_h} \mathbf{f}^1 \cdot \mathbf{z}\, dx, \qquad \forall \mathbf{z} \in \mathbf{W}_{0h}, \qquad \mathbf{y}_h^1 \in \mathbf{W}_h, \tag{60}$$

$$\mathbf{y}_h^1 = \mathbf{y}_\infty \qquad \text{on } \Gamma_{\mathrm{u},h} \cup \Gamma_{\mathrm{N},h} \cup \Gamma_{\mathrm{S},h}, \tag{61}$$

$$\mathbf{y}_h^1 = \mathbf{v}^1 \qquad \text{on } \partial B_h; \tag{62}$$

then for $n = 2, \ldots, N$,

$$\rho \int_{\Omega_h} \frac{(3/2)\mathbf{y}_h^n - 2\mathbf{y}_h^{n-1} + (1/2)\mathbf{y}_h^{n-2}}{\Delta t} \cdot \mathbf{z}\, dx + 2\mu \int_{\Omega_h} \mathbf{D}(\mathbf{y}_h^n) : \mathbf{D}(\mathbf{z})\, dx$$
$$+ \rho \int_{\Omega_h} \left((2\mathbf{y}_h^{n-1} - \mathbf{y}_h^{n-2}) \cdot \nabla\right)(2\mathbf{y}_h^{n-1} - \mathbf{y}_h^{n-2}) \cdot \mathbf{z}\, dx$$
$$= \rho \int_{\Omega_h} \mathbf{f}^n \cdot \mathbf{z}\, dx, \qquad \forall \mathbf{z} \in \mathbf{W}_{0h}, \qquad \mathbf{y}_h^n \in \mathbf{W}_h, \tag{63}$$

$$\mathbf{y}_h^n = \mathbf{y}_\infty \qquad \text{on } \Gamma_{\mathrm{u},h} \cup \Gamma_{\mathrm{N},h} \cup \Gamma_{\mathrm{S},h}, \tag{64}$$

$$\mathbf{y}_h^n = \mathbf{v}^n \qquad \text{on } \partial B_h. \tag{65}$$

The pressure unknown has been eliminated, at the price of having to use finite element spaces defined by nontrivial linear constraints and also the necessity to construct vector bases of $\mathbf{W}_h$ and $\mathbf{W}_{0h}$ satisfying these constraints. For more details on approximately divergence-free element spaces and the construction of the corresponding basis (shape) functions see, e.g., Chapter VI in [6] (and the references therein).

4.3. *Formulation of the Fully Discrete Control Problem*

Using the above approximation of the Navier–Stokes equations yields the discrete control problem

$$\begin{aligned} \mathbf{u}_h^{\Delta t} &\in \mathcal{U}_h^{\Delta t}, \\ J_h^{\Delta t}\big(\mathbf{u}_h^{\Delta t}\big) &\le J_h^{\Delta t}(\mathbf{v}), \qquad \forall \mathbf{v} \in \mathcal{U}_h^{\Delta t}, \end{aligned} \tag{66}$$

with

$$\mathcal{U}_h^{\Delta t} = \boldsymbol{\Lambda}_h^N, \tag{67}$$

$$\boldsymbol{\Lambda}_h = \left\{ \boldsymbol{\lambda} \,\middle|\, \int_{\partial B} \boldsymbol{\lambda} \cdot \mathbf{n}\, ds = 0,\ \boldsymbol{\lambda} = \tilde{\boldsymbol{\lambda}}\Big|_{\partial B},\ \tilde{\boldsymbol{\lambda}} \in \mathbf{W}_h \right\}, \tag{68}$$

and

$$J_h^{\Delta t}(\mathbf{v}) = \frac{\epsilon}{2}\,\Delta t \left(\sum_{n=1}^{N} \|\mathbf{v}^n\|_\alpha^2 + \sum_{n=2}^{N} \left\| \frac{\mathbf{v}^n - \mathbf{v}^{n-1}}{\Delta t} \right\|_0^2 \right) + \Delta t \sum_{n=1}^{N} P_{\mathrm{d},h}^n, \tag{69}$$

where the discrete drag power $P_{\mathrm{d},h}^n$ is defined by

$$\begin{aligned} P_{\mathrm{d},h}^1 = {} & \rho \int_{\Omega_h} \frac{\mathbf{y}_h^1 - \mathbf{y}_h^0}{\Delta t} \cdot \mathbf{y}_b^1\, dx + 2\mu \int_{\Omega_h} \mathbf{D}\left(\frac{2}{3}\mathbf{y}_h^1 + \frac{1}{3}\mathbf{y}_h^0 \right) : \mathbf{D}\big(\mathbf{y}_b^1\big)\, dx \\ & + \rho \int_{\Omega_h} \big(\mathbf{y}_h^0 \cdot \nabla\big)\mathbf{y}_h^0 \cdot \mathbf{y}_b^1\, dx - \rho \int_{\Omega_h} \mathbf{f}^1 \cdot \mathbf{y}_b^1\, dx, \end{aligned} \tag{70}$$

and for $n = 2, \ldots, N$

$$\begin{aligned} P_{\mathrm{d},h}^n = {} & \rho \int_{\Omega_h} \frac{(3/2)\mathbf{y}_h^n - 2\mathbf{y}_h^{n-1} + (1/2)\mathbf{y}_h^{n-2}}{\Delta t} \cdot \mathbf{y}_b^n\, dx + 2\mu \int_{\Omega_h} \mathbf{D}\big(\mathbf{y}_h^n\big) : \mathbf{D}\big(\mathbf{y}_b^n\big)\, dx \\ & + \rho \int_{\Omega_h} \big(\big(2\mathbf{y}_h^{n-1} - \mathbf{y}_h^{n-2}\big) \cdot \nabla\big)\big(2\mathbf{y}_h^{n-1} - \mathbf{y}_h^{n-2}\big) \cdot \mathbf{y}_b^n\, dx - \rho \int_{\Omega_h} \mathbf{f}^n \cdot \mathbf{y}_b^n\, dx, \end{aligned} \tag{71}$$

with $\mathbf{y}_b^n$ a "lifting" (i.e., an extension) of $\mathbf{v}^n - \mathbf{y}_\infty$, contained in $\mathbf{W}_h$ and vanishing on $\Gamma_{\mathrm{u},h} \cup \Gamma_{\mathrm{N},h} \cup \Gamma_{\mathrm{S},h}$. The above quantities approximate P_{d}^n defined in Section 3.2. In (70) and (71), $\{\mathbf{y}_h^n\}_{n=0}^N$ is obtained from $\mathbf{v}^n$ via the solution of (59)–(65).

Remark 4.1. Using the facts that $\mathbf{y}_h^n$ and $\mathbf{y}_b^n$ are approximately divergence-free, that $\mathbf{y}_b^n$ vanishes away from ∂B, and that $\mathbf{y}_h^n$ satisfies the discrete momentum equations (59)–(65), it can be shown that the relations (70) and (71) are discrete analogues of the drag power (10). For more details on the variational approximation of boundary fluxes in the context of the Navier–Stokes equations, see, e.g., [16, 35].

5. GRADIENT CALCULATION

Computing the gradient $\nabla J_h^{\Delta t}$ of functional $J_h^{\Delta t}$ is at the same time straightforward and complicated; let us comment on this apparently paradoxical statement: computing the gradient is straightforward in the sense that it relies on a well-established and systematical methodology which has been discussed in many articles (see, e.g., [4, 12, 13, 20, 21]); on the other hand the relative complication of the discrete state equations (59)–(65) makes the calculation of $\nabla J_h^{\Delta t}$ a bit tedious as we can guess from the relations just below. Indeed, the gradient $\nabla J_h^{\Delta t}(\mathbf{v})$ of functional $J_h^{\Delta t}$ at $\mathbf{v}$ is given by

$$\left\langle \nabla J_h^{\Delta t}(\mathbf{v}),\ \mathbf{w} \right\rangle = \Delta t \sum_{n=1}^{N} \left\langle \mathbf{g}_h^n - \frac{\mathbf{n} \int_{\partial B} \mathbf{g}_h^n \cdot \mathbf{n}\, ds}{\int_{\partial B} ds},\ \mathbf{w}^n \right\rangle, \qquad \forall \mathbf{w} \in \mathcal{U}_h^{\Delta t}, \tag{72}$$

with

$$\begin{aligned}
\left\langle \mathbf{g}_h^N,\ \mathbf{w}^N \right\rangle = {} & \epsilon(\mathbf{v}^N, \mathbf{w}^N)_\alpha + \epsilon\left(\frac{\mathbf{v}^N - \mathbf{v}^{N-1}}{(\Delta t)^2}, \mathbf{w}^N \right) + \rho \int_{\Omega_h} \frac{(3/2)\mathbf{p}_h^N}{\Delta t} \cdot \tilde{\mathbf{w}}^N \, dx \\
& + 2\mu \int_{\Omega_h} \mathbf{D}\left(\mathbf{p}_h^N\right) : \mathbf{D}(\tilde{\mathbf{w}}^N)\, dx + \rho \int_{\Omega_h} \frac{(3/2)\mathbf{y}_h^N - 2\mathbf{y}_h^{N-1} + (1/2)\mathbf{y}_h^{N-2}}{\Delta t} \cdot \tilde{\mathbf{w}}^N \, dx \\
& + \rho \int_{\Omega_h} \left[\left(2\mathbf{y}_h^{N-1} - \mathbf{y}_h^{N-2}\right) \cdot \nabla \right] \left(2\mathbf{y}_h^{N-1} - \mathbf{y}_h^{N-2}\right) \cdot \tilde{\mathbf{w}}^N \, dx \\
& + 2\mu \int_{\Omega_h} \mathbf{D}\left(\mathbf{y}_h^N\right) : \mathbf{D}(\tilde{\mathbf{w}}^N)\, dx - \rho \int_{\Omega_h} \mathbf{f}_h^N \cdot \tilde{\mathbf{w}}^N \, dx,
\end{aligned} \tag{73}$$

and

$$\begin{aligned}
\left\langle \mathbf{g}_h^{N-1}, \mathbf{w}^{N-1} \right\rangle = {} & \epsilon(\mathbf{v}^{N-1}, \mathbf{w}^{N-1})_\alpha + \epsilon\left(\frac{2\mathbf{v}^{N-1} - \mathbf{v}^{N-2} - \mathbf{v}^N}{(\Delta t)^2}, \mathbf{w}^{N-1} \right) \\
& + \rho \int_{\Omega_h} \frac{(3/2)\mathbf{p}_h^{N-1} - 2\mathbf{p}_h^N}{\Delta t} \cdot \tilde{\mathbf{w}}^{N-1} \, dx + 2\mu \int_{\Omega_h} \mathbf{D}\left(\mathbf{p}_h^{N-1}\right) : \mathbf{D}(\tilde{\mathbf{w}}^{N-1})\, dx \\
& + \rho \int_{\Omega_h} \left[\left(2\mathbf{y}_h^{N-1} - \mathbf{y}_h^{N-2}\right) \cdot \nabla \right] (\tilde{\mathbf{w}}^{N-1}) \cdot \left(2\mathbf{p}_h^N\right) dx \\
& + \rho \int_{\Omega_h} (\tilde{\mathbf{w}}^{N-1} \cdot \nabla) \left(2\mathbf{y}_h^{N-1} - \mathbf{y}_h^{N-2}\right) \cdot \left(2\mathbf{p}_h^N\right) dx \\
& + \rho \int_{\Omega_h} \frac{(3/2)\mathbf{y}_h^{N-1} - 2\mathbf{y}_h^{N-2} + (1/2)\mathbf{y}_h^{N-3}}{\Delta t} \cdot \tilde{\mathbf{w}}^{N-1} \, dx \\
& + \rho \int_{\Omega_h} \left[\left(2\mathbf{y}_h^{N-2} - \mathbf{y}_h^{N-3}\right) \cdot \nabla \right] \left(2\mathbf{y}_h^{N-2} - \mathbf{y}_h^{N-3}\right) \cdot (\tilde{\mathbf{w}}^{N-1})\, dx \\
& + 2\mu \int_{\Omega_h} \mathbf{D}\left(\mathbf{y}_h^{N-1}\right) : \mathbf{D}(\tilde{\mathbf{w}}^{N-1})\, dx - \rho \int_{\Omega_h} \mathbf{f}_h^{N-1} \cdot \tilde{\mathbf{w}}^{N-1} \, dx,
\end{aligned} \tag{74}$$

then for $n = N-2, \dots, 2$,

$$\begin{aligned}
\langle \mathbf{g}_h^n, \mathbf{w}^n \rangle &= \epsilon(\mathbf{v}^n, \mathbf{w}^n)_\alpha + \epsilon\left(\frac{2\mathbf{v}^n - \mathbf{v}^{n-1} - \mathbf{v}^{n+1}}{(\Delta t)^2}, \mathbf{w}^n\right) \\
&\quad + \rho \int_{\Omega_h} \frac{(3/2)\mathbf{p}_h^n - 2\mathbf{p}_h^{n+1} + (1/2)\mathbf{p}_h^{n+2}}{\Delta t} \cdot \tilde{\mathbf{w}}^n \, dx + 2\mu \int_{\Omega_h} \mathbf{D}\big(\mathbf{p}_h^n\big) : \mathbf{D}(\tilde{\mathbf{w}}^n) \, dx \\
&\quad + \rho \int_{\Omega_h} \big[\big(2\mathbf{y}_h^n - \mathbf{y}_h^{n-1}\big) \cdot \nabla\big](\tilde{\mathbf{w}}^n) \cdot \big(2\mathbf{p}_h^{n+1}\big) \, dx \\
&\quad + \rho \int_{\Omega_h} \big[\big(2\mathbf{y}_h^{n+1} - \mathbf{y}_h^n\big) \cdot \nabla\big](\tilde{\mathbf{w}}^n) \cdot \big(-\mathbf{p}_h^{n+2}\big) \, dx \\
&\quad + \rho \int_{\Omega_h} (\tilde{\mathbf{w}}^n \cdot \nabla)\big(2\mathbf{y}_h^n - \mathbf{y}_h^{n-1}\big) \cdot \big(2\mathbf{p}_h^{n+1}\big) \, dx \\
&\quad + \rho \int_{\Omega_h} (\tilde{\mathbf{w}}^n \cdot \nabla)\big(2\mathbf{y}_h^{n+1} - \mathbf{y}_h^n\big) \cdot \big(-\mathbf{p}_h^{n+2}\big) \, dx \\
&\quad + \rho \int_{\Omega_h} \frac{(3/2)\mathbf{y}_h^n - 2\mathbf{y}_h^{n-1} + (1/2)\mathbf{y}_h^{n-2}}{\Delta t} \cdot \tilde{\mathbf{w}}^n \, dx \\
&\quad + \rho \int_{\Omega_h} \big[\big(2\mathbf{y}_h^{n-1} - \mathbf{y}_h^{n-2}\big) \cdot \nabla\big]\big(2\mathbf{y}_h^{n-1} - \mathbf{y}_h^{n-2}\big) \cdot (\tilde{\mathbf{w}}^n) \, dx \\
&\quad + 2\mu \int_{\Omega_h} \mathbf{D}\big(\mathbf{y}_h^n\big) : \mathbf{D}(\tilde{\mathbf{w}}^n) \, dx - \rho \int_{\Omega_h} \mathbf{f}_h^n \cdot \tilde{\mathbf{w}}^n \, dx, \qquad (75)
\end{aligned}$$

and, finally, for $n = 1$,

$$\begin{aligned}
\langle \mathbf{g}_h^1, \mathbf{w}^1 \rangle &= \epsilon(\mathbf{v}^1, \mathbf{w}^1)_\alpha + \epsilon\left(\frac{\mathbf{v}^1 - \mathbf{v}^2}{(\Delta t)^2}, \mathbf{w}^1\right) \\
&\quad + \rho \int_{\Omega_h} \frac{\mathbf{p}_h^1 - 2\mathbf{p}_h^2 + (1/2)\mathbf{p}_h^3}{\Delta t} \cdot \tilde{\mathbf{w}}^1 \, dx + 2\mu \int_{\Omega_h} \mathbf{D}\left(\frac{2}{3}\mathbf{p}_h^1\right) : \mathbf{D}(\tilde{\mathbf{w}}^1) \, dx \\
&\quad + \rho \int_{\Omega_h} \big[\big(2\mathbf{y}_h^1 - \mathbf{y}_h^0\big) \cdot \nabla\big](\tilde{\mathbf{w}}^1) \cdot \big(2\mathbf{p}_h^2\big) \, dx \\
&\quad + \rho \int_{\Omega_h} \big[\big(2\mathbf{y}_h^2 - \mathbf{y}_h^1\big) \cdot \nabla\big](\tilde{\mathbf{w}}^1) \cdot \big(-\mathbf{p}_h^3\big) \, dx \\
&\quad + \rho \int_{\Omega_h} (\tilde{\mathbf{w}}^1 \cdot \nabla)\big(2\mathbf{y}_h^1 - \mathbf{y}_h^0\big) \cdot \big(2\mathbf{p}_h^2\big) \, dx \\
&\quad + \rho \int_{\Omega_h} (\tilde{\mathbf{w}}^1 \cdot \nabla)\big(2\mathbf{y}_h^2 - \mathbf{y}_h^1\big) \cdot \big(-\mathbf{p}_h^3\big) \, dx \\
&\quad + \rho \int_{\Omega_h} \frac{\mathbf{y}_h^1 - \mathbf{y}_h^0}{\Delta t} \cdot \tilde{\mathbf{w}}^1 \, dx + \rho \int_{\Omega_h} \big(\mathbf{y}_h^0 \cdot \nabla\big)\big(\mathbf{y}_h^0\big) \cdot (\tilde{\mathbf{w}}^1) \, dx \\
&\quad + 2\mu \int_{\Omega_h} \mathbf{D}\left(\frac{2}{3}\mathbf{y}_h^1 + \frac{1}{3}\mathbf{y}_h^0\right) : \mathbf{D}(\tilde{\mathbf{w}}^1) \, dx - \rho \int_{\Omega_h} \mathbf{f}_h^1 \cdot \tilde{\mathbf{w}}^1 \, dx. \qquad (76)
\end{aligned}$$

In (73)–(76) $\tilde{\mathbf{w}}^n$ is a lifting of $\mathbf{w}^n$ contained in $\mathbf{W}_h$ and vanishing on $\Gamma_{\mathrm{u},h} \cup \Gamma_{\mathrm{N},h} \cup \Gamma_{\mathrm{S},h}$, and $\mathbf{p}_h^n \in \mathbf{W}_h$ is the solution of the discrete adjoint system

$$\rho \int_{\Omega_h} \frac{(3/2)\mathbf{p}_h^N}{\Delta t} \cdot \mathbf{z}\, dx + 2\mu \int_{\Omega_h} \mathbf{D}\big(\mathbf{p}_h^N\big) : \mathbf{D}(\mathbf{z})\, dx = 0, \qquad \forall \mathbf{z} \in \mathbf{W}_{0h}, \tag{77}$$

$$\mathbf{p}_h^N = \mathbf{0} \qquad \text{on } \boldsymbol{\Gamma}_{\mathrm{u},h} \cup \boldsymbol{\Gamma}_{\mathrm{N},h} \cup \boldsymbol{\Gamma}_{\mathrm{S},h}, \tag{78}$$

$$\mathbf{p}_h^N = \mathbf{v}_h^N - \mathbf{y}_\infty \qquad \text{on } \partial B_h; \tag{79}$$

and

$$\begin{aligned} &\rho \int_{\Omega_h} \frac{(3/2)\mathbf{p}_h^{N-1} - 2\mathbf{p}_h^N}{\Delta t} \cdot \mathbf{z}\, dx + 2\mu \int_{\Omega_h} \mathbf{D}\big(\mathbf{p}_h^{N-1}\big) : \mathbf{D}(\mathbf{z})\, dx \\ &\quad + \rho \int_{\Omega_h} \big[\big(2\mathbf{y}_h^{N-1} - \mathbf{y}_h^{N-2}\big) \cdot \nabla\big]\mathbf{z} \cdot \big(2\mathbf{p}_h^N\big)\, dx \\ &\quad + \rho \int_{\Omega_h} (\mathbf{z} \cdot \nabla)\big(2\mathbf{y}_h^{N-1} - \mathbf{y}_h^{N-2}\big) \cdot \big(2\mathbf{p}_h^N\big)\, dx = 0, \qquad \forall \mathbf{z} \in \mathbf{W}_{0h}, \end{aligned} \tag{80}$$

$$\mathbf{p}_h^{N-1} = \mathbf{0} \qquad \text{on } \boldsymbol{\Gamma}_{\mathrm{u},h} \cup \boldsymbol{\Gamma}_{\mathrm{N},h} \cup \boldsymbol{\Gamma}_{\mathrm{S},h}, \tag{81}$$

$$\mathbf{p}_h^{N-1} = \mathbf{v}_h^{N-1} - \mathbf{y}_\infty \qquad \text{on } \partial B_h; \tag{82}$$

then for $n = N-2, \ldots, 2$,

$$\begin{aligned} &\rho \int_{\Omega_h} \frac{(3/2)\mathbf{p}_h^n - 2\mathbf{p}_h^{n+1} + (1/2)\mathbf{p}_h^{n+2}}{\Delta t} \cdot \mathbf{z}\, dx + 2\mu \int_{\Omega_h} \mathbf{D}\big(\mathbf{p}_h^n\big) : \mathbf{D}(\mathbf{z})\, dx \\ &\quad + \rho \int_{\Omega_h} \big[\big(2\mathbf{y}_h^n - \mathbf{y}_h^{n-1}\big) \cdot \nabla\big]\mathbf{z} \cdot \big(2\mathbf{p}_h^{n+1}\big)\, dx \\ &\quad + \rho \int_{\Omega_h} \big[\big(2\mathbf{y}_h^{n+1} - \mathbf{y}_h^n\big) \cdot \nabla\big]\mathbf{z} \cdot \big(-\mathbf{p}_h^{n+2}\big)\, dx \\ &\quad + \rho \int_{\Omega_h} (\mathbf{z} \cdot \nabla)\big(2\mathbf{y}_h^n - \mathbf{y}_h^{n-1}\big) \cdot \big(2\mathbf{p}_h^{n+1}\big)\, dx \\ &\quad + \rho \int_{\Omega_h} (\mathbf{z} \cdot \nabla)\big(2\mathbf{y}_h^{n+1} - \mathbf{y}_h^n\big) \cdot \big(-\mathbf{p}_h^{n+2}\big)\, dx = 0, \qquad \forall \mathbf{z} \in \mathbf{W}_{0h}, \end{aligned} \tag{83}$$

$$\mathbf{p}_h^n = \mathbf{0} \qquad \text{on } \boldsymbol{\Gamma}_{\mathrm{u},h} \cup \boldsymbol{\Gamma}_{\mathrm{N},h} \cup \boldsymbol{\Gamma}_{\mathrm{S},h}, \tag{84}$$

$$\mathbf{p}_h^n = \mathbf{v}_h^n - \mathbf{y}_\infty \qquad \text{on } \partial B_h; \tag{85}$$

and, finally, for $n = 1$,

$$\begin{aligned} &\rho \int_{\Omega_h} \frac{\mathbf{p}_h^1 - 2\mathbf{p}_h^2 + (1/2)\mathbf{p}_h^3}{\Delta t} \cdot \mathbf{z}\, dx + 2\mu \int_{\Omega_h} \mathbf{D}\left(\frac{2}{3}\mathbf{p}_h^1\right) : \mathbf{D}(\mathbf{z})\, dx \\ &\quad + \rho \int_{\Omega_h} \big[\big(2\mathbf{y}_h^1 - \mathbf{y}_h^0\big) \cdot \nabla\big]\mathbf{z} \cdot \big(2\mathbf{p}_h^2\big)\, dx \\ &\quad + \rho \int_{\Omega_h} \big[\big(2\mathbf{y}_h^2 - \mathbf{y}_h^1\big) \cdot \nabla\big]\mathbf{z} \cdot \big(-\mathbf{p}_h^3\big)\, dx \end{aligned}$$

$$+\rho\int_{\Omega_h}(\mathbf{z}\cdot\nabla)\big(2\mathbf{y}_h^1-\mathbf{y}_h^0\big)\cdot\big(2\mathbf{p}_h^2\big)\,dx$$

$$+\rho\int_{\Omega_h}(\mathbf{z}\cdot\nabla)\big(2\mathbf{y}_h^2-\mathbf{y}_h^1\big)\cdot\big(-\mathbf{p}_h^3\big)\,dx=0,\qquad\forall\mathbf{z}\in\mathbf{W}_{0h},\tag{86}$$

$$\mathbf{p}_h^1=\mathbf{0}\qquad\text{on }\boldsymbol{\Gamma}_{\mathrm{u},h}\cup\boldsymbol{\Gamma}_{\mathrm{N},h}\cup\boldsymbol{\Gamma}_{\mathrm{S},h},\tag{87}$$

$$\mathbf{p}_h^1=\mathbf{v}_h^1-\mathbf{y}_\infty\qquad\text{on }\partial B_h.\tag{88}$$

Once $\nabla J_h^{\Delta t}$ is known, via the solution of the above adjoint system, we can derive optimality conditions which enable us to solve the discrete control problem (66) by various kinds of descent methods such as conjugate gradient, BFGS, etc. The BFGS solution of (66) will be discussed in Section 6 hereafter.

Remark 5.1. As observed by one of the referees the term $((\mathbf{v}^N-\mathbf{v}^{N-1})/(\Delta t)^2,\mathbf{w}^N)$ (resp., $((\mathbf{v}^1-\mathbf{v}^2)/(\Delta t)^2,\mathbf{w}^1)$) in (73) (resp., in (76)) can be interpreted as $((2\mathbf{v}^N-\mathbf{v}^{N-1}-\mathbf{v}^{N+1})/(\Delta t)^2,\mathbf{w}^N)$ (resp., $((2\mathbf{v}^1-\mathbf{v}^0-\mathbf{v}^2)/(\Delta t)^2,\mathbf{w}^1)$) completed by $\mathbf{v}^N=\mathbf{v}^{N+1}$ (resp., $\mathbf{v}^1=\mathbf{v}^0$), i.e., by the discrete analogues of $\partial_t\mathbf{v}|_{t=0}=\partial_t\mathbf{v}|_{t=T}=\mathbf{0}$, natural boundary conditions associated to the functional $\int_0^T\int_{\partial B}|\partial_t\mathbf{v}(x,t)|^2\,ds\,dt$.

6. A BFGS ALGORITHM FOR THE DISCRETE CONTROL PROBLEM

In order to solve the discrete control problem (66) we shall employ a *quasi-Newton method* à la BFGS (see, e.g., [27] for BFGS algorithms and their implementation); such an algorithm reads as follows when applied to the solution of a generic optimization problem such as

$$\begin{aligned}&x\in\mathbb{R}^l,\\ &f(x)\le f(y),\ \forall y\in\mathbb{R}^l.\end{aligned}\tag{89}$$

If f is smooth enough the solution of problem (89) satisfies also

$$\nabla f(x)=0.\tag{90}$$

The BFGS algorithm applied to the solution of (89), (90) takes the form

$$x^0\in\mathbb{R}^l,\ H^0\in\mathcal{L}(\mathbb{R}^l,\mathbb{R}^l)\text{ are given},\tag{91}$$

$$g^0=\nabla f(x^0).\tag{92}$$

For $k\ge0$, assuming that x^k, H^k, and g^k are known, we proceed as follows:

$$d^k=-H^kg^k;\tag{93}$$

find $\rho_k\in\mathbb{R}$, such that

$$f(x^k+\rho_kd^k)\le f(x^k+\rho d^k),\qquad\forall\rho\in\mathbb{R};\tag{94}$$

$$x^{k+1}=x^k+\rho_kd^k;\tag{95}$$

$$g^{k+1}=\nabla f(x^{k+1});\tag{96}$$

$$s^k = x^{k+1} - x^k; \tag{97}$$

$$y^k = g^{k+1} - g^k; \tag{98}$$

$$H^{k+1} = H^k + \frac{(s^k - H^k y^k) \otimes s^k + s^k \otimes (s^k - H^k y^k)}{(y^k, s^k)} - \frac{(s^k - H^k y^k, y^k)}{(y^k, s^k)^2} s^k \otimes s^k. \tag{99}$$

Set $k = k + 1$ and return to (93).

The tensor product of two vectors u and v in $\mathbb{R}^l$ is defined, as usual, as the linear mapping from $\mathbb{R}^l \times \mathbb{R}^l$ into $\mathbb{R}^l$ such that

$$(u \otimes v)w = (v, w)u, \quad \forall w \in \mathbb{R}^l. \tag{100}$$

In (99), (100), we have denoted by $(\cdot, \cdot)$ the Euclidean scalar product used on space $\mathbb{R}^l$; $(\cdot, \cdot)$ is not necessarily the dot product on $\mathbb{R}^l$, since we may have $(v, w) = Sv \cdot w, \forall v, w \in \mathbb{R}^l$, with S a $l \times l$ matrix, symmetric and positive definite. In fact, we have used a discrete analogue of $-d^2/dt^2 + I$ as preconditioner, the associated boundary conditions (in time) being of the homogeneous Neumann type.

Applying the above algorithm to the solution of the discrete control problem (66) is straightforward.

7. VALIDATION OF THE FLOW SIMULATOR

7.1. *Motivation*

An important issue for the flow control problem discussed in this article is the quality of the flow simulator, i.e., of the methodology which will be used to solve the Navier–Stokes equations modeling the flow (and also the adjoint equations) in order to compute $\nabla J_h^{\Delta t}$. For the validation of our flow simulator we have chosen as test problem the flow past a circular cylinder at various Reynolds numbers. This test problem has the advantage of combining a simple geometry with a rich flow dynamics and it has always been a traditional benchmarking problem for incompressible viscous flow simulators (see, e.g., [1, 3, 5, 24] and the many references therein). Also, this particular geometry has motivated the work of several flow investigators from the experimental points of view (see, e.g., [33, 36, 37]).

7.2. *Description of the Mesh and Other Parameters*

In order to validate our incompressible viscous flow simulator we have chosen as computational domain the two-dimensional region Ω,

$$\Omega = \Pi \backslash \bar{B},$$

where Π is the rectangle $(-15, 45) \times (-15, 15)$ and B is the disk of center $(0, 0)$ and of radius $a = 0.5$. The diameter of B will be taken as characteristic length, implying that the Reynolds number is defined as

$$\mathrm{Re} = \frac{2a\rho|\mathbf{y}_\infty|}{\mu}.$$

The simulations will be done with $\mu = 1/200$ and $1/1000$, implying that $\mathrm{Re} = 200$ and 1000, for $\rho = 1$. The finite element mesh used for the calculations at $\mathrm{Re} = 1000$ is shown in

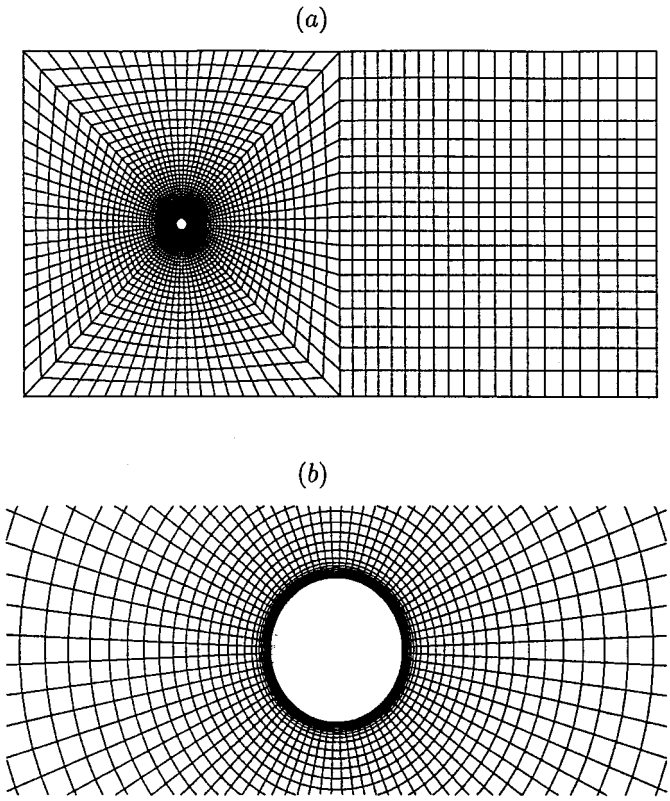

FIG. 2. (a) Mesh used for Reynolds number 1000 and (b) its elements in the neighborhood of B.

Fig. 2, where we have also visualized the mesh in the neighborhood of B. When oscillatory rotations are performed an attached layer with high velocity gradients is formed around the cylinder, forcing us to construct attached layers of elements close to the cylinder. Outside the layers of attached elements, the radial mesh spacing was chosen to scale with the Reynolds number, assuming that the boundary layer thickness varies like $1/\sqrt{\mathrm{Re}}$. Next, further away from the cylinder the mesh was stretched gradually to fit the rectangular shape of the computational domain. Actually further information for both $\mathrm{Re} = 200$ and $\mathrm{Re} = 1000$ calculations is provided in Table I.

7.3. *Numerical Results and Comparisons*

The goal of these computational experiments is to simulate the development of the vortex street in an unforced laminar wake behind the circular cylinder in Fig. 2, for $\mathrm{Re} = 200$ and 1000. Although the simulations at $\mathrm{Re} = 1000$ are two-dimensional and they do not include the effects of 3D instabilities and turbulence, the high Re 2D simulations are still of interest

TABLE I
Discretization Parameters

Re	Δt	Elements	Points	Nodes	Unknowns
200	0.005	2226	2297	9,046	11,415
1000	0.001	4104	4200	16,608	20,905

in comparing with other 2D results and in capturing the key dynamics of the large, 2D vortices, which clearly dominate the high Re flow experiments such as those of Tokumaru and Dimotakis.

Actually, for Re values below 40–50 a stable steady flow is observed with formation of a bubble in the wake. The length of the recirculating zone increases with Re, and beyond a certain critical value the flow becomes unstable. Alternating eddies are formed in an asymmetrical pattern which generates an alternating separation of vortices. These vortices are advected and diffused downstream, forming the well-known Karman vortex street. In "actual life" symmetry breaking is triggered by various causes such as disturbances in the initial and/or boundary conditions. In our simulation the computational mesh and the boundary conditions are perfectly symmetric. As an initial condition we have taken the symmetric solution obtained from a Navier–Stokes calculation where symmetry is systematically enforced at each time step by averaging. This symmetric solution (unstable for Re sufficiently large) is itself used as initial condition for a simulation where the symmetry constraint has been relaxed. The symmetry breaking taking place for Re sufficiently large can be explained by the various truncation and rounding errors taking place in the calculations.

At the initial stage of the symmetry breaking, the growth of the perturbation is linear and the drag coefficient grows very fast at first up to a point where the growth becomes oscillating and saturation is observed. In Figs. 3 and 4 we present the variations of the drag and the lift versus t for $\mathrm{Re} = 200$ and 1000, respectively. The periodic regime which is reached asymptotically is characterized by the frequency at which the vortices are shed. A

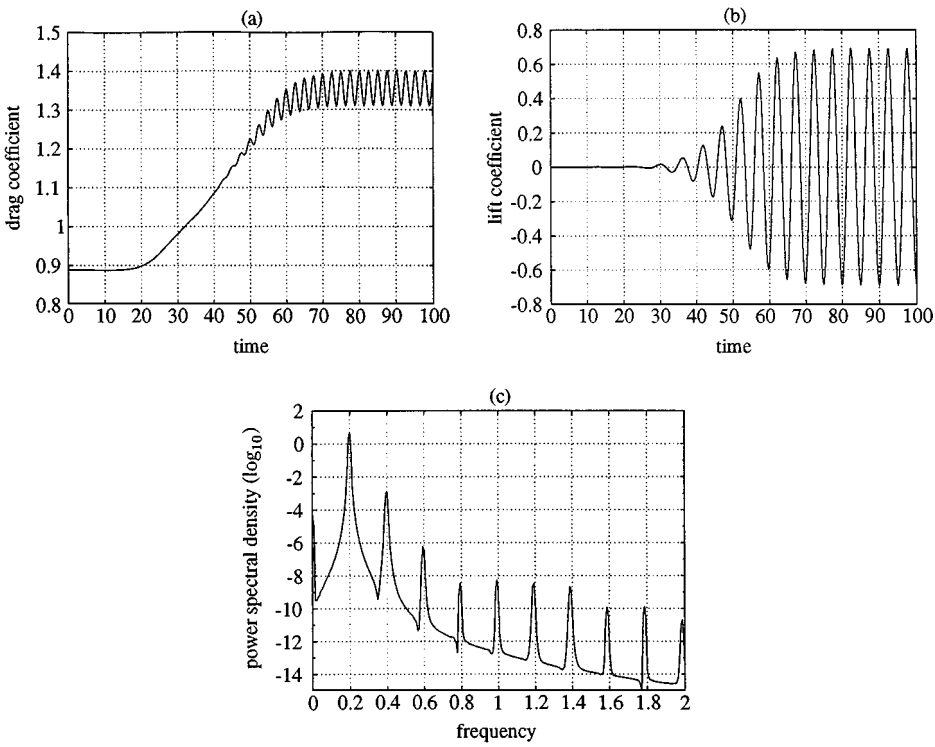

FIG. 3. Case of a fixed cylinder in uniform free-stream flow, Re = 200. (a) Drag and (b) lift coefficient. (c) Power spectrum density of the lift coefficient history. The Strouhal number is 0.1978.

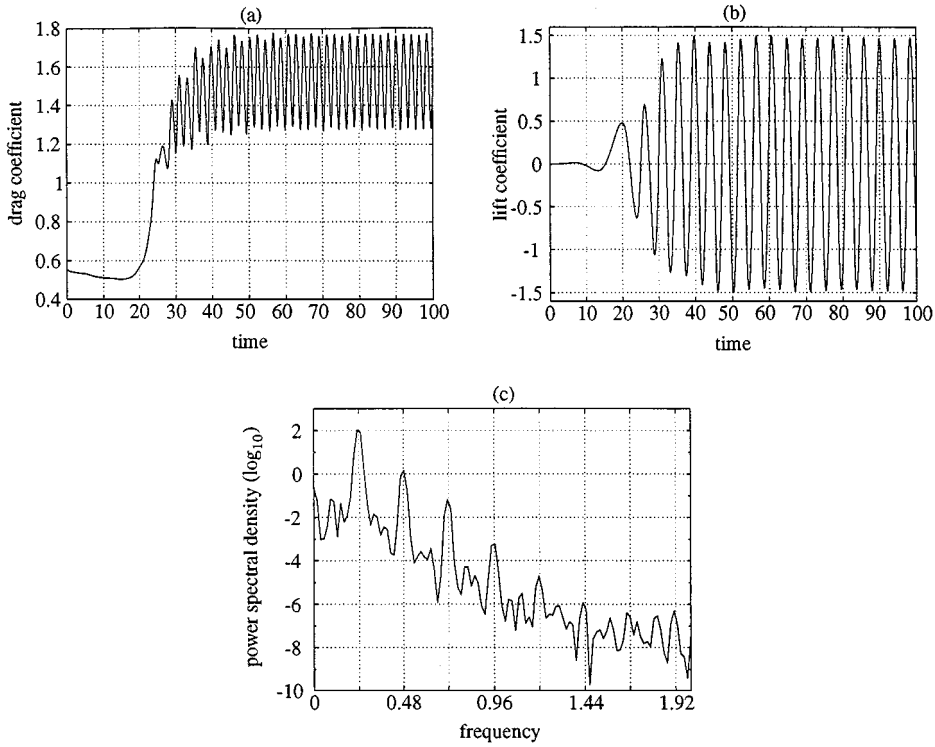

FIG. 4. Case of a fixed cylinder in uniform free-stream flow, Re = 1000. (a) Drag and (b) lift coefficient. (c) Power spectrum of the lift coefficient history. The Strouhal number is 0.2392.

spectral analysis of the lift was performed on a time interval of 30 periods, after subtraction of the mean drag. The behavior of the drag was found to be predominantly harmonic with a fundamental frequency much stronger than its superharmonics; see Figs. 3c and 4c for the power spectrum of the lift coefficient history at Re = 200 and 1000, respectively (the power spectral density calculation done in this article has been computed using the methods described in [31]).

For comparison purposes it was found convenient to introduce the *Strouhal* number

$$S_n = \frac{2a}{|\mathbf{y}_\infty|} f_n,$$

which is a nondimensional representation of the shedding frequency. In Table II, a comparison is given at various Re between the Strouhal numbers from our simulation and those obtained experimentally and computationally by various authors ([2, 27, 33, 37]). The agreement with Henderson's computational data and Williamson's experimental data is very good for Re between 60 and 1000. For more details on these comparisons see [28]. Similarly, in Table III, the time-averaged drag coefficient is seen to be in very good agreement with Henderson's results for the steady and periodic state [22]. However, the results of Braza *et al.* [2] are inconsistent for Reynolds number 1000 and do not match other two-dimensional simulations. A well-known effect of having just two dimensions in numerical simulations as opposed to three is that the drag tends to be overpredicted for higher Reynolds numbers, where three-dimensional instabilities would occur. For more details on these drag comparisons see, again, [28].

TABLE II
Strouhal Numbers for Various Reynolds Numbers

	S_n				
Re	Present work	Henderson [22]	Williamson [37]	Roshko [32]	Braza *et al.* [5]
60	0.1353	0.1379	0.1356	0.1370	—
80	0.1526	0.1547	0.1521	0.1557	—
100	0.1670	0.1664	0.1640	0.1670	0.16
200	0.1978	0.1971	—	—	0.20
400	0.2207	0.2198	—	—	—
600	0.2306	0.2294	—	—	—
800	0.2353	0.2343	—	—	—
1000	0.2392	0.2372	—	—	0.21

8. ACTIVE CONTROL BY ROTATION: NUMERICAL RESULTS

8.1. *Synopsis*

In this section we investigate via simulation various strategies for the active control by rotation of the flow around a cylinder. In Section 8.2 we consider the dynamical behavior of the flow under the effect of forced sinusoidal rotation of the cylinder. Then in Section 8.3 we present the results obtained when applying the optimal control strategy discussed in Sections 2 to 6.

8.2. *Active Control by Forced Sinusoidal Rotation*

The active control discussed in this section is based on *oscillatory rotation* as in the experiments of Tokumaru and Dimotakis [36]. If the forcing is *sinusoidal* there are *two degrees of freedom*, namely the *frequency* f_e and the *amplitude* ω_1 of the angular velocity. The forcing Strouhal number is defined as

$$S_e = 2af_e/|\mathbf{y}_\infty|,$$

TABLE III
Drag Coefficients for Various Reynolds Numbers

	C_D			
Re	Present work	Henderson [22]	Braza *et al.* [5]	Fornberg [9]
20	2.0064	2.0587	2.19	2.0001
40	1.5047	1.5445	1.58	1.4980
60	1.3859	1.4151	1.35	—
80	1.3489	1.3727	—	—
100	1.3528	1.3500	1.36	—
200	1.3560	1.3412	1.39	—
400	1.4232	1.4142	—	—
600	1.4641	1.4682	—	—
800	1.4979	1.4966	—	—
1000	1.5191	1.5091	1.198	—

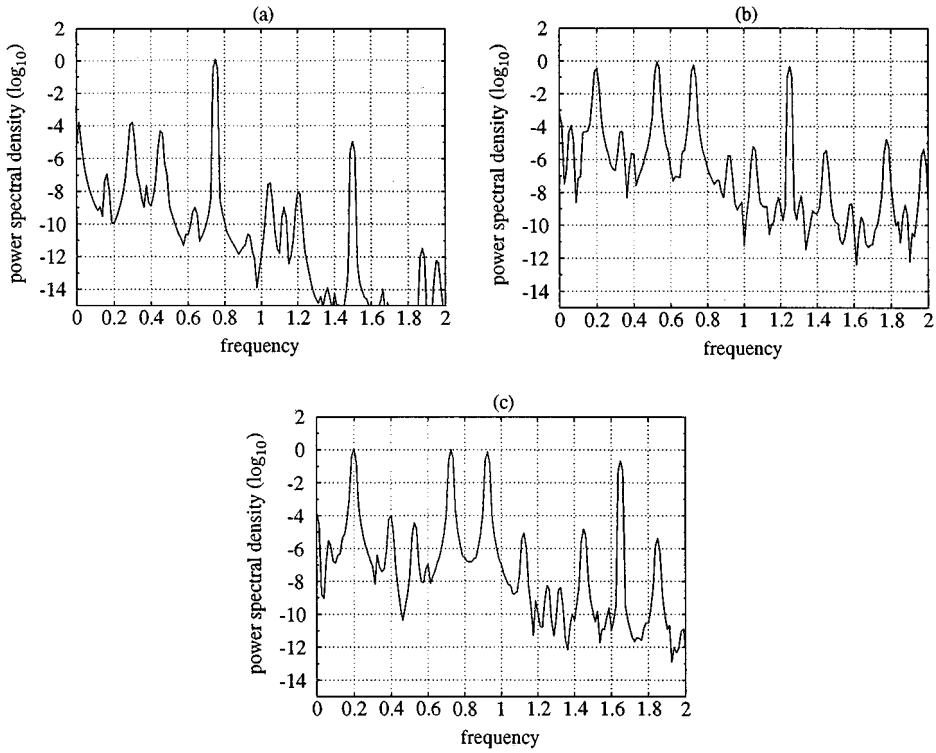

FIG. 5. Case of a sinusoidal rotating cylinder in uniform free-stream flow, Re = 200. Power spectral density of the lift coefficient history is shown for (a) lock-in ($S_e = 0.75$), (b) quasiperiodic ($S_e = 1.25$), and (c) nonreceptive state ($S_e = 1.65$). The natural Strouhal number (S_n) is 0.1978.

which yields the forcing angular velocity

$$\omega(t) = \omega_1 \sin(2\pi S_e t).$$

A series of simulations with different forcing frequencies S_e varying from 0.35 to 1.65 was performed at Re = 200. The amplitude ω_1 of the forcing angular velocity was held fixed to the value 6 for all simulations. Once the transients had died out, a spectral analysis of the (time-dependent) drag minus its time-averaged value was performed, leading to the results shown in Figs. 5a, 5b, and 5c, which correspond to $S_e = 0.75$, 1.25, and 1.65, respectively. Several comments are in order:

1. At $S_e = 0.75$ a perfect lock-in to the forcing frequency can be observed, in which the forcing frequency dominates the dynamics of the flow (in simple terms: *the flow oscillates at the forcing frequency*).

2. At $S_e = 1.25$, there is competition between the forcing frequency and the natural shedding fundamental frequency. The dynamics corresponds to a quasi-periodic state.

3. At $S_e = 1.65$ the flow dynamics is dominated by the natural shedding frequency (0.2 from Table II); the forcing frequency has little influence on the flow dynamics.

These results agree with those in [26], which discusses the active control of flow around cylinders by sinusoidal transversal motions (a kind of chattering control).

Similar experiments were performed at Re = 1000, with $\omega_1 = 5.5$ and $S_e = 0.625$, 1.325, and 1.425. The corresponding results are reported in Figs. 6a, 6b, and 6c. The computed

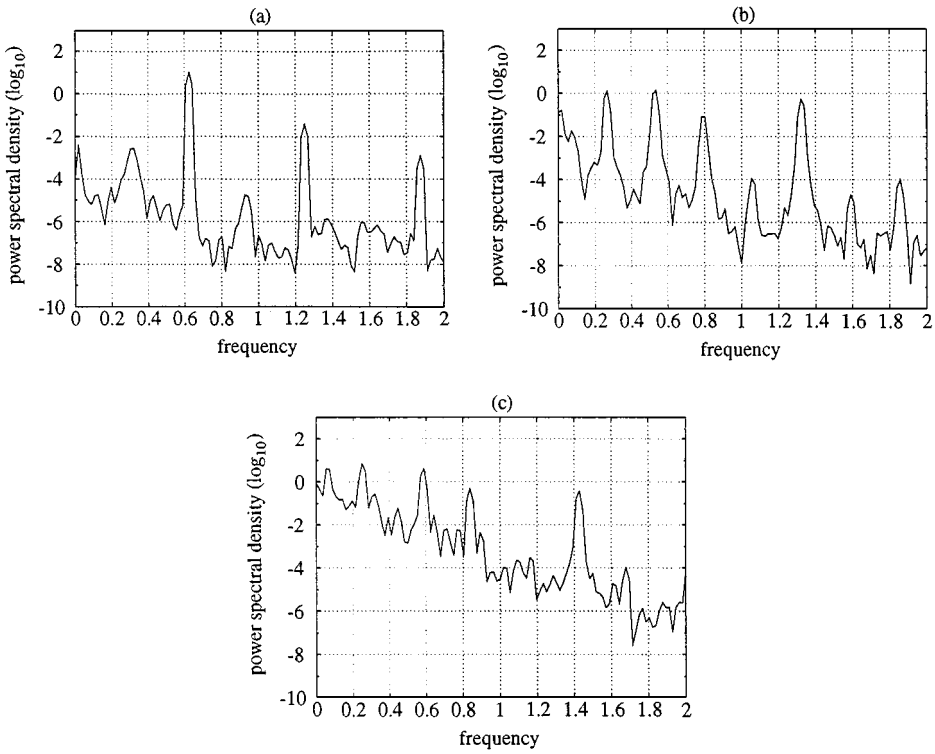

FIG. 6. Case of a sinusoidal rotating cylinder in uniform free-stream flow, $\mathrm{Re} = 1000$. Power spectral density of the lift coefficient history for (a) lock-in ($S_e = 0.625$), (b) quasiperiodic ($S_e = 1.325$), and (c) nonreceptive state ($S_e = 1.425$). The natural Strouhal number (S_n) is 0.2392.

results suggest the existence of a threshold amplitude for the forcing; we need to operate beyond this threshold for the flow to "feel" the forcing. It was further observed that this threshold is a function of the forcing frequency: higher frequencies require higher amplitude for the control to stay effective.

The above results suggest looking for *optimal pairs* $\{\omega_1, S_e\}$ for *drag minimization*. To be more precise, we consider the drag as a function of $\{\omega_1, S_e\}$ and try to minimize this function for $\{\omega_1, S_e\}$ varying in a "reasonable" subset of $\mathbb{R}^2$. For $\mathrm{Re} = 200$ a method coupling *direct search* and BFGS algorithms yields $\omega_1 = 6$ and $S_e = 0.74$, which corresponds to the lock-in case previously described. In Fig. 7 we visualize the contours of the drag, considered as a function of ω_1 and S_e, in the neighborhood of the optimal solution. In Fig. 8a we show the variation versus time of the optimal sinusoidal control whose action started at time $t = 0$. The transition to low drag is visualized in Fig. 8b, which also shows the shedding frequency transition. The drag reduction was found to be on the order of 30%. The lift coefficient is presented in Fig. 8c; we observe that the amplitude of the lift oscillations is substantially reduced. Finally in Figs. 9a and 9b we show snapshots of the uncontrolled flow and of the optimally forced flow. The significant vortex-shedding phenomenon observed in Fig. 9a has been substantially reduced and the flow has been quasi-symmetrized. This is qualitatively similar to the effects observed by Tokumaru and Dimotakis [36]. Details of the vortex shedding for various values of t are reported in Fig. 10; these figures clearly show the important reduction of vortex shedding in the cylinder wake.

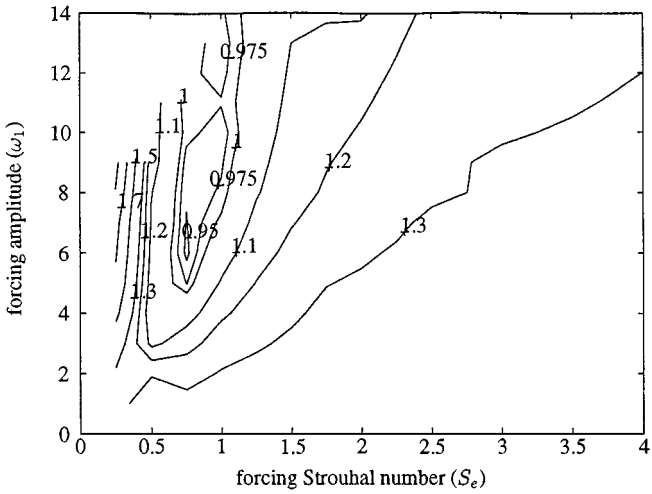

FIG. 7. Variation of the drag C_D with S_e and ω_1 at Reynolds number 200.

Similar experiments have been carried out for $\mathrm{Re} = 1000$. Qualitatively, the simulated phenomena are identical to those observed for $\mathrm{Re} = 200$; however, the drag reduction this time is on the order of 60%. The optimal amplitude and frequency are, this time, $\omega_1 = 5.5$ and $S_e = 0.625$. The results shown in Figs. 11 to 14 are self-explanatory.

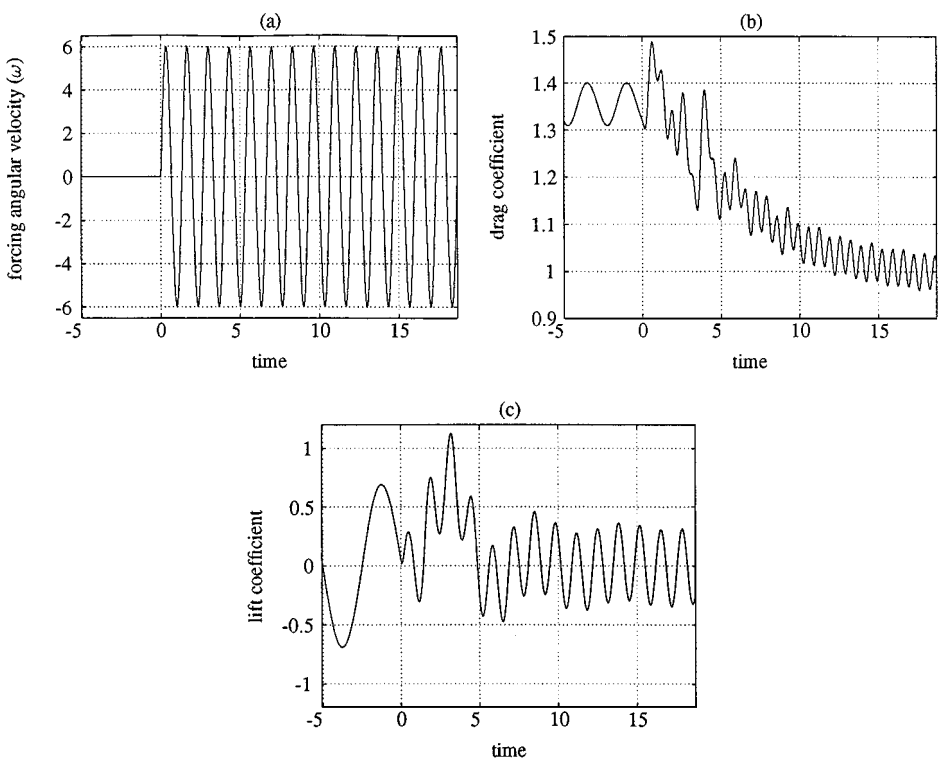

FIG. 8. The time evolution of the (a) sinusoidal-optimal forcing, with $S_e = 0.75$ and $\omega_1 = 6.00$, (b) drag C_D, and (c) lift C_L, at Reynolds number 200. Forcing was started at time $t = 0$.

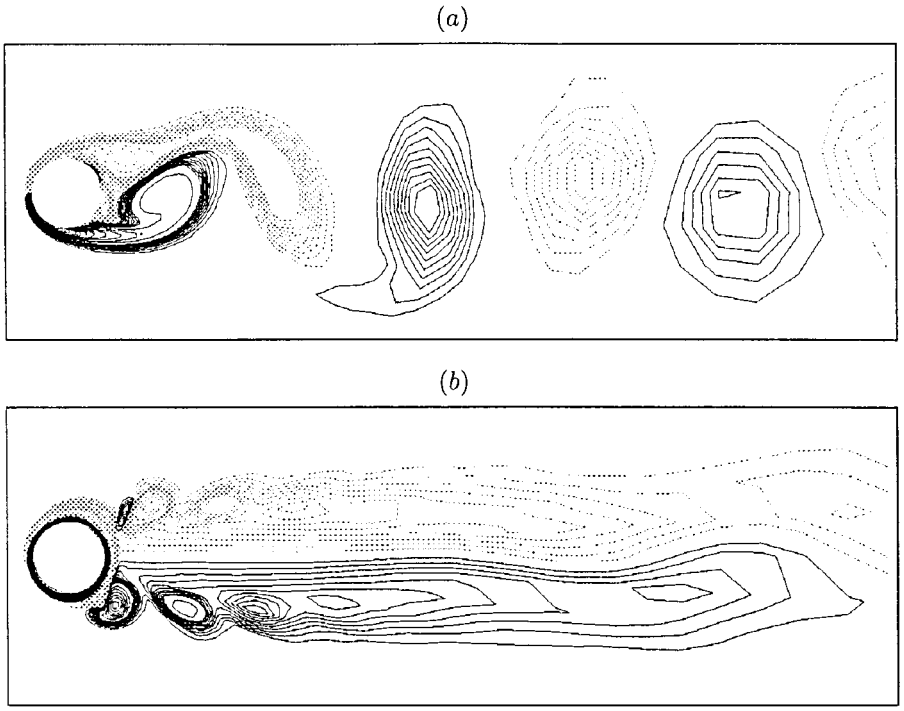

FIG. 9. Vorticity contour plot of the wake of the unforced (a) and forced (b) flow at Reynolds number 200.

8.3. *Drag Reduction by Optimal Control*

In this section we present the results obtained by applying the methods discussed in Sections 2 to 6 to active flow control by rotation, the cost function being essentially the drag, since the following results have been obtained with $\epsilon = 0$ in (2.9). The values of Re are as in Section 8.2, namely 200 and 1000. The discretization parameters are also chosen as in Section 8.2. As initial guess for the optimal control computation we have used the quasi-optimal forcing obtained in Section 8.2. Typically convergence was obtained in 20 iterations of the BFGS algorithm for

$$\frac{(g^{k+1}, g^{k+1})}{(g^0, g^0)} \leq 10^{-6}.$$

Let us comment first on the result obtained for $\mathrm{Re} = 200$. In Fig. 15a we represent the computed optimal control (—) as a function of t and compare it to the optimal sinusoidal control (—) obtained in Section 8.2. We observe that the fundamental frequency of the optimal control is very close to the optimal frequency for the sinusoidal control. The power spectral density of the optimal control is shown in Fig. 15b.

Similarly, we present in Figs. 16a and 16b the results corresponding to $\mathrm{Re} = 1000$. From these figures we observe that the fundamental frequency of the optimal control and the optimal frequency for the sinusoidal control are even closer than for $\mathrm{Re} = 200$.

From these simulations it follows that:

1. The fundamental frequency of the optimal control is very close to the optimal frequency obtained by the methods of Section 8.2.

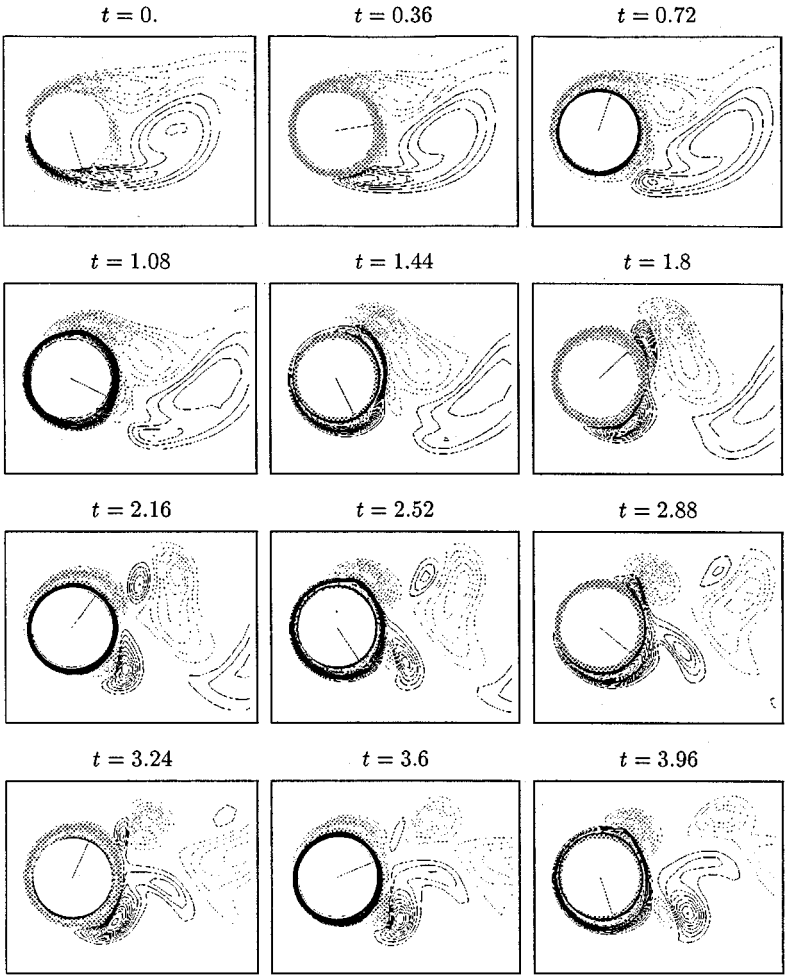

FIG. 10. Near-wake region: Forced vortex shedding at Reynolds number 200 with $S_e = 0.75$ and $\omega_1 = 6$. The sequence represents the first three forcing period.

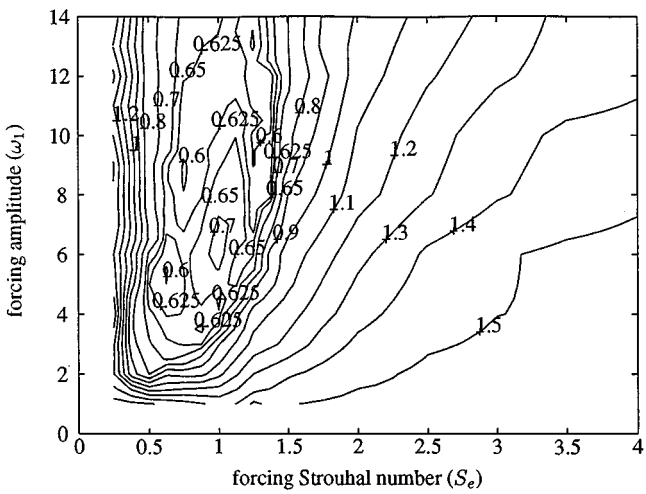

FIG. 11. Variation of the drag C_D with S_e and ω_1 at Reynolds number 1000.

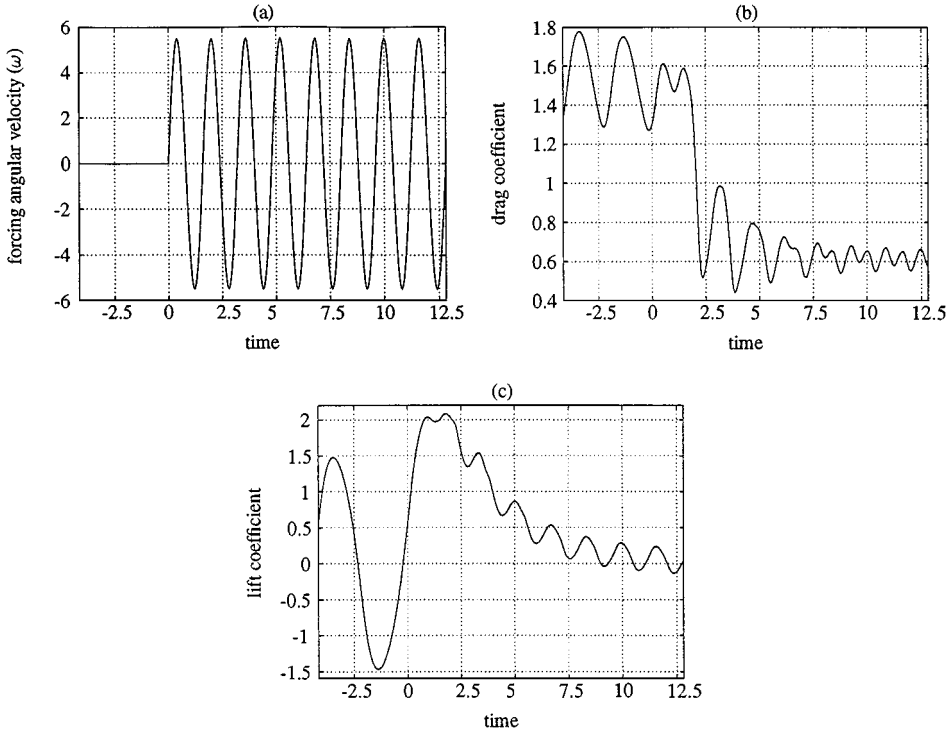

FIG. 12. The time evolution of the (a) sinusoidal-optimal forcing, with $S_e = 0.625$ and $\omega_1 = 5.5$, (b) drag C_D and (c) lift C_L, at Reynolds number 1000. Forcing was started at time $t = 0$.

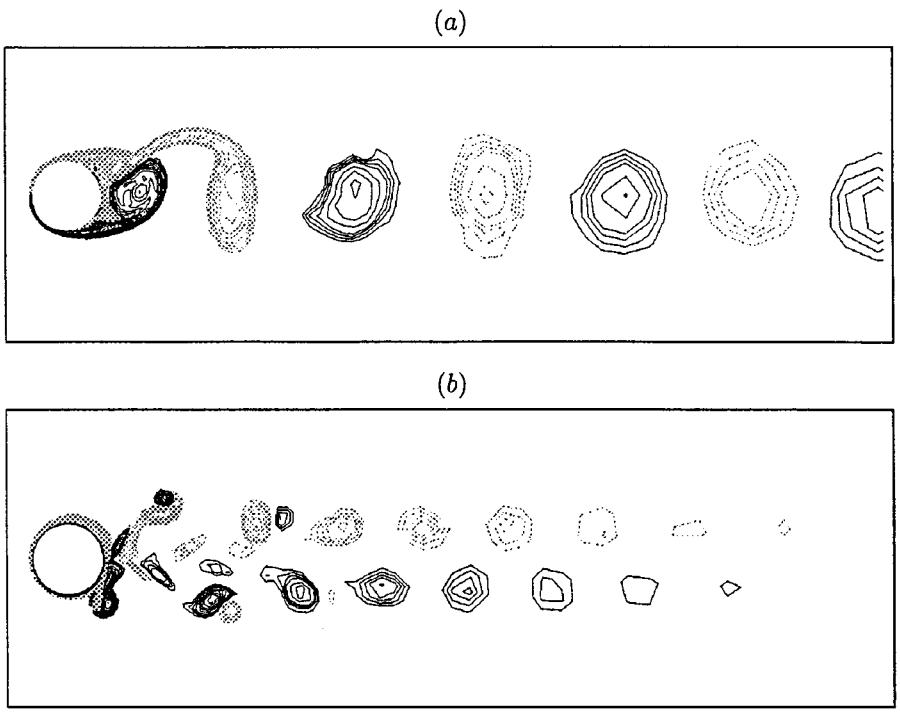

FIG. 13. Vorticity contour plot of the wake of the unforced (a) and forced (b) flow at Reynolds number 1000.

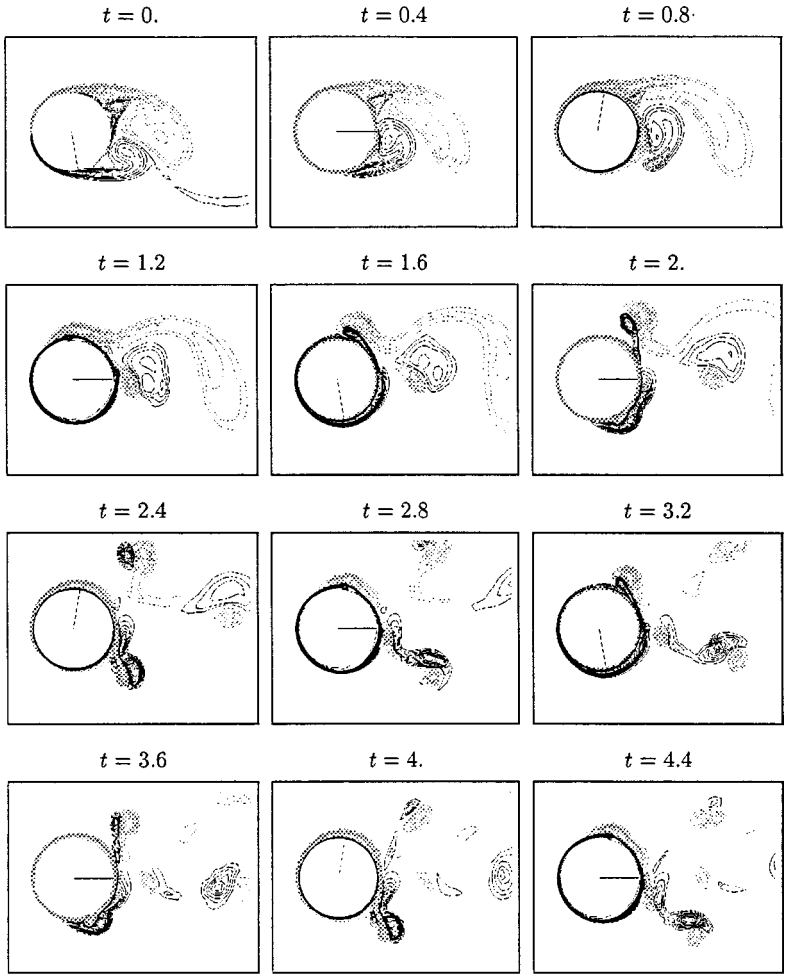

FIG. 14. Near-wake region: Vortex shedding frequency shifted from its natural shedding frequency ($S_n = 0.2398$) to the forcing frequency ($S_e = 0.625$), Re = 1000 and $\omega_1 = 5.5$. The sequence represents the first three forcing period.

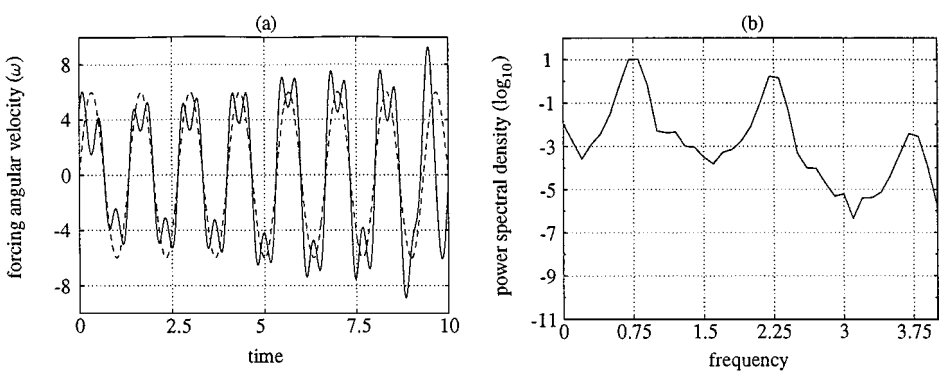

FIG. 15. The (a) optimal forcing at Reynolds number 200 and its (b) power spectral density. In (a) the dashed line represents the optimal sinusoidal control.

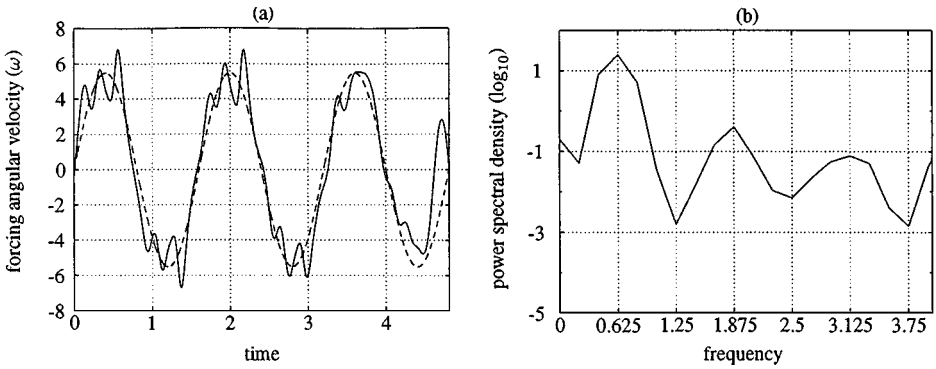

FIG. 16. The (a) optimal periodic forcing at Reynolds number 1000 and its (b) power spectral density. In (a) the dashed line represents the optimal sinusoidal control.

2. The optimal control has one fundamental frequency and several harmonics whose frequencies are *odd* multiples of the fundamental frequency.

8.4. *Drag Reduction by Control in Fourier Space*

From the results described in Section 8.3, it appears that the optimal controls obtained there were predominantly composed of a sinusoidal mode oscillating at a fundamental frequency superposed with higher harmonic modes. This observation suggests looking for the controls in Fourier space. More precisely the angular velocity $\omega(t)$ will be of the form

$$\omega(t) = \sum_{k=1}^{K} \omega_k \sin(2k\pi S_e t - \delta_k). \tag{101}$$

At $\mathrm{Re} = 200$, in order to see what effect additional harmonics may have on the drag reduction, the optimal forcing was sought in the space described by (101) with three different values of K, namely 1, 3, and 10. The time interval for the control $(0, T)$ was chosen so that $T = 3T_f$, with $T_f = 1/S_e$ the forcing period. A piecewise optimal control strategy was used for the solution of the periodic control problem; to be more precise, the control time interval $(0, T)$ was divided into sub-intervals of equal length and the optimal control methodology previously discussed was applied successively on each of these sub-intervals. Computational results show that the effect of the phase shifts δ_i is small, suggesting taking $\delta_k = 0$ in (101).

The computational experiment reported in Figs. 17–19 corresponds to the following scenario:

- From $t = -T$ to $t = 0$, the cylinder is fixed, there is no control, and the flow oscillates at its natural frequency.
- At $t = 0$ control starts with optimal periodic control in the class given by relation (105).

The optimal periodic control with $K = 1$ (resp., $K = 3$, $K = 10$) is shown in Fig. 17a (resp., 18a, 19a) and its corresponding drag and lift are shown in Figs. 17b and 17c (resp., 18b and 18c, 19b and 19c). The highly oscillatory controls, drag, and lift observed in Figs. 17–19 as K increases can be explained by the fact that they were computed with $\epsilon = 0$ in the cost

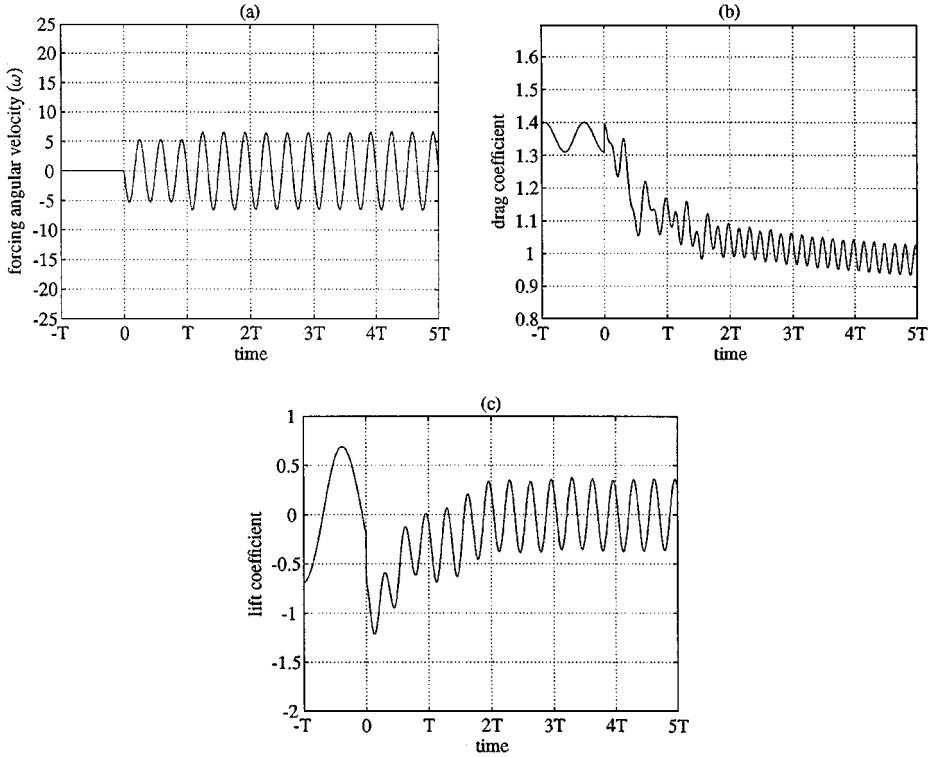

FIG. 17. The (a) optimal periodic control, (b) the corresponding drag, and (c) the corresponding lift. $K = 1$.

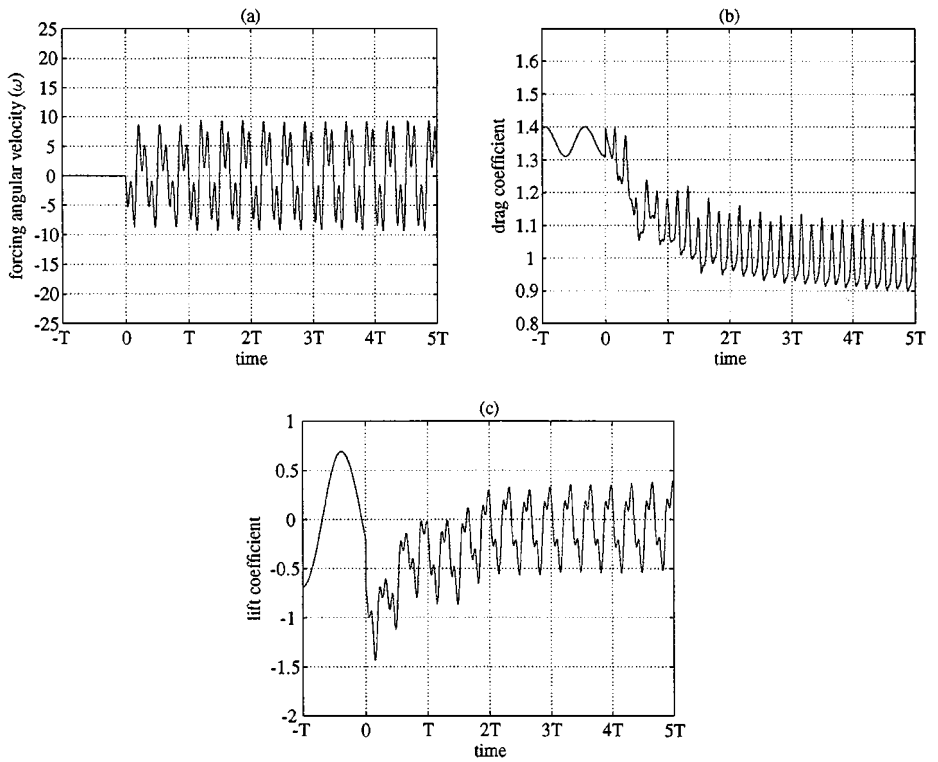

FIG. 18. The (a) optimal periodic control, (b) the corresponding drag, and (c) the corresponding lift. $K = 3$.

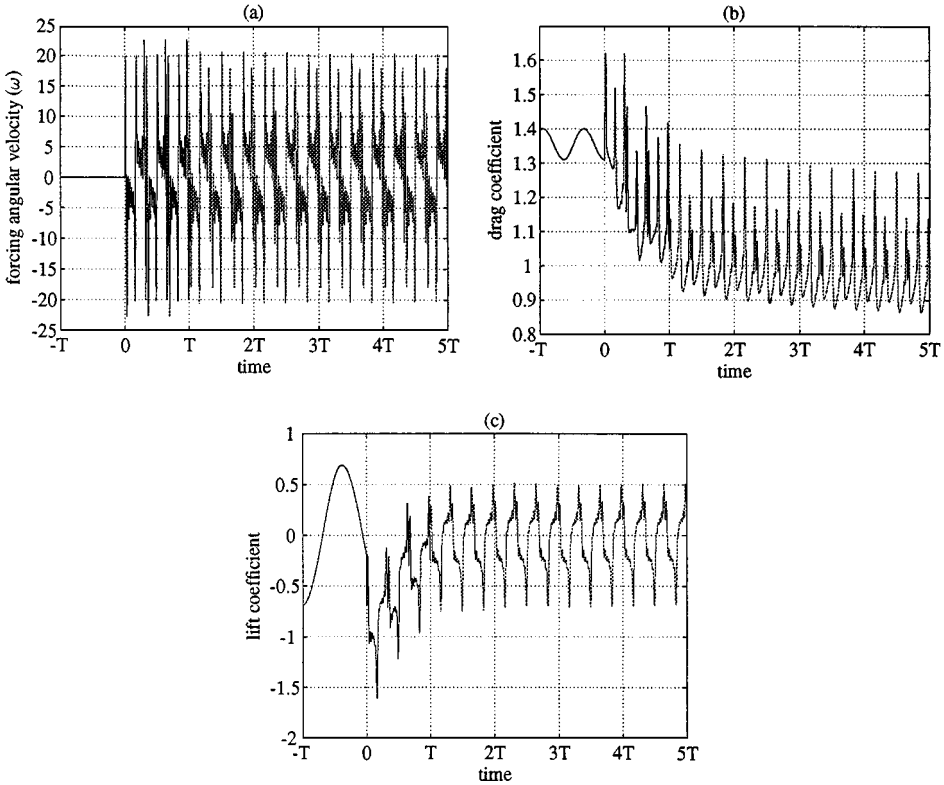

FIG. 19. The (a) optimal periodic control, (b) the corresponding drag, and (c) the corresponding lift. $K = 10$.

function (9); introducing a positive regularization parameter ϵ into the cost function would have the immediate effect of smoothing the above results.

The optimal periodic control obtained during the 10th piecewise control loop has been used successfully to stabilize the system beyond that loop; the effectiveness of this approach relies on the fact that most transient effects have been damped out. A deeper analysis of the

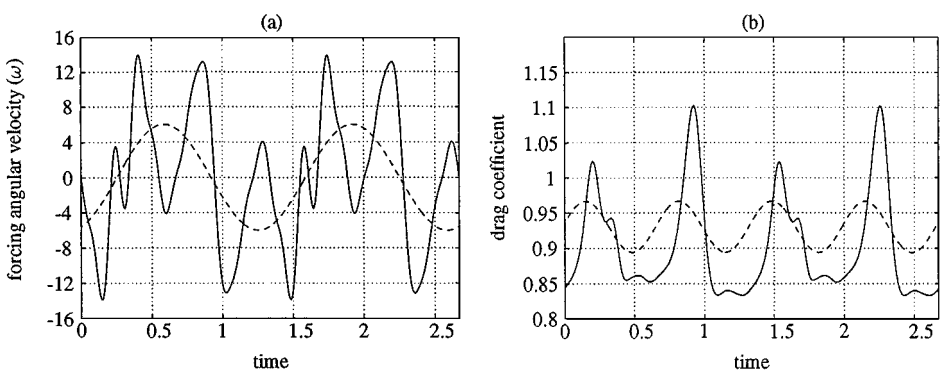

FIG. 20. The (a) optimal periodic control (solid) in comparison with the optimal sinusoidal (dashed) control at Reynolds number 200. In (b) the corresponding drag is shown, with an additional reduction of 2.9% from the optimal sinusoidal forced case.

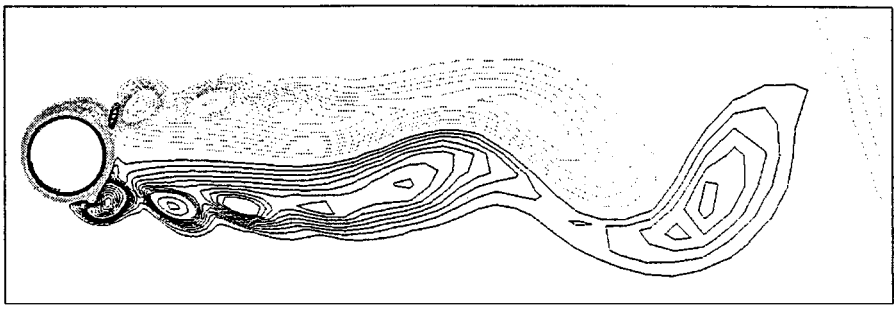

FIG. 21. Vorticity contour plot of the wake of the optimally forced flow at Reynolds number 200.

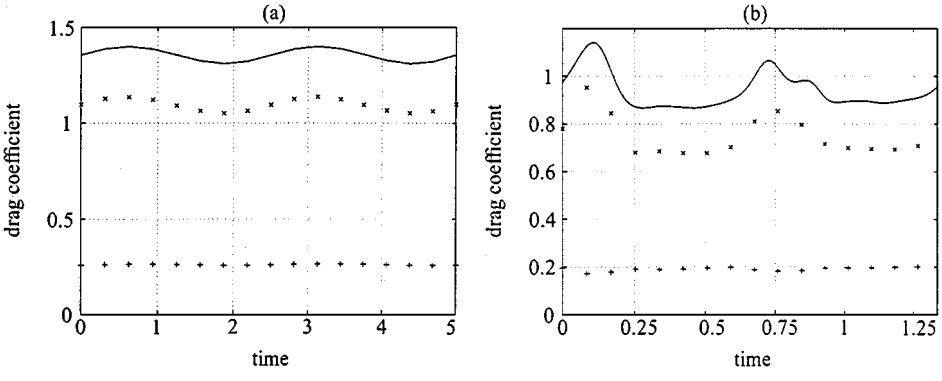

FIG. 22. The time evolution of the drag and its viscous and pressure components for (a) the unforced and (b) the optimal periodic forced case, at Reynolds number 200. The total drag is represented by a solid line and the pressure and viscosity components by $\times$ and $+$ respectively.

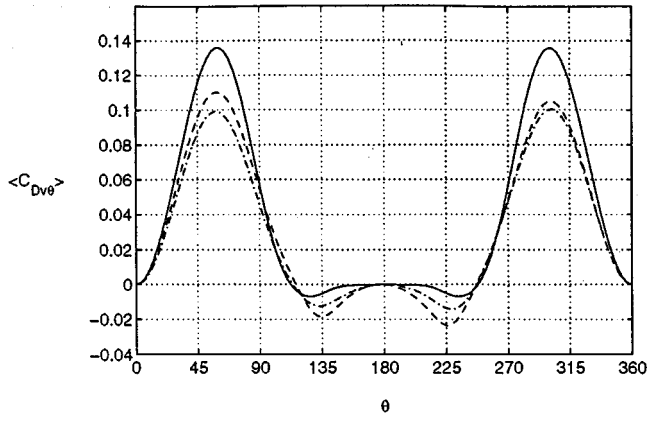

FIG. 23. Contribution of the time-averaged viscous drag as a function of the angle, at Reynolds number 200. The solid line represents the unforced case, the dashed line the optimal sinusoidal forced case, and the dash–dotted line the optimal periodic forced case.

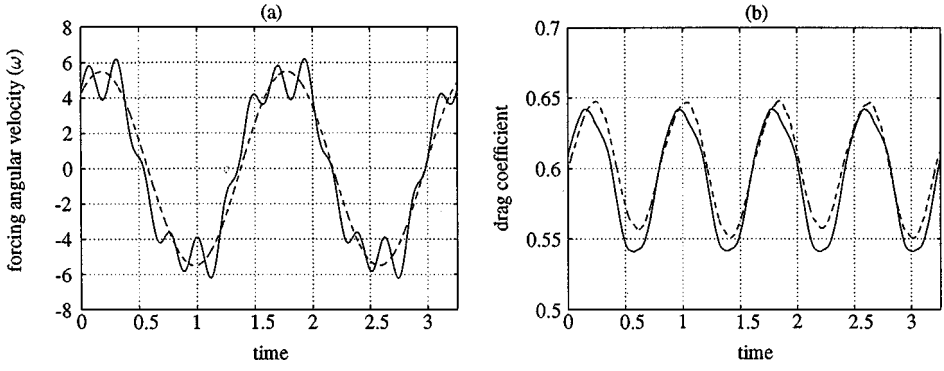

FIG. 24. The (a) optimal forcing (solid) in comparison with the quasi-optimal (dashed) forcing at Reynolds number 1000. In (b) the corresponding drag is shown, with an additional reduction of 1.5% from the quasi-optimally forced case.

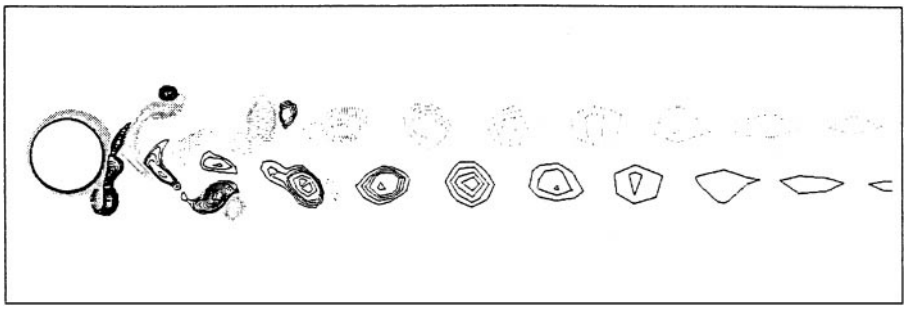

FIG. 25. Vorticity contour plot of the wake of the optimally forced flow at Reynolds number 1000.

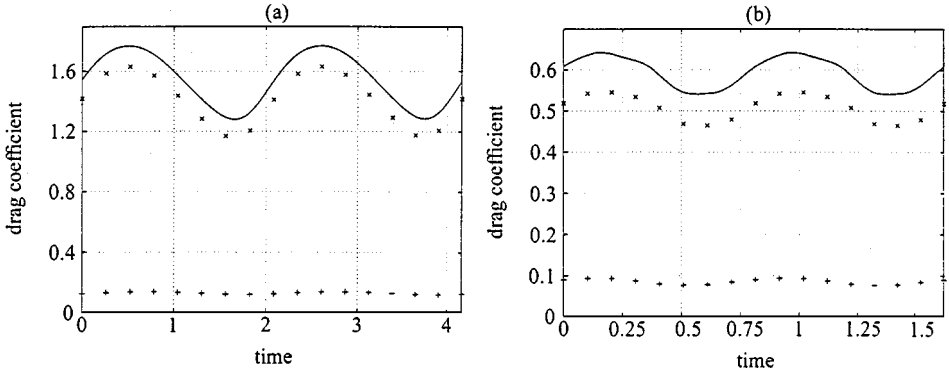

FIG. 26. The time evolution of the drag and its viscous and pressure components for (a) the unforced and (b) the optimal periodic forced case, at Reynolds number 1000. The total drag is represented by a solid line and the pressure and viscosity components by $\times$ and $+$ respectively.

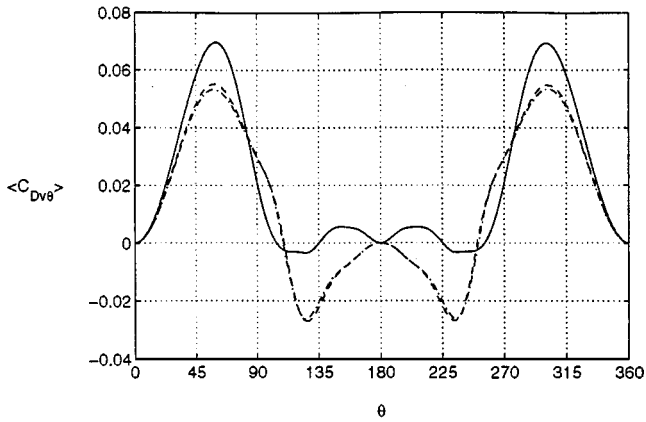

FIG. 27. Contribution of the time-averaged viscous drag as a function of the angle, at Reynolds number 1000. The solid line represents the unforced case, the dashed line the forced case, and the dash–dotted line the optimally forced case.

optimal periodic state reached with $K = 5$ is in order. From Fig. 20, we observe that when the peak rotation speed is reached, a corresponding minimum in the drag occurs, at times $t = 0.6$, $t = 1.25$, and $t = 1.9$. We observe that the effect of the optimal control is to flatten the drag in the neighborhood of its minima and to sharpen it in the neighborhood of the maxima. This can be seen in Fig. 20b at times $t = 0.5$, $t = 1.15$, and $t = 1.85$. Indeed, the sharp peaks in the drag correspond to times when the forcing changes direction, i.e., crosses zero. A very interesting feature can be seen at times $t = 0.2$ and $t = 1.5$, where a zig-zag forcing motion corresponds to a lower peak in the drag. This optimization of the periodic forcing leads to an extra reduction in the drag coefficient from 0.932 to 0.905, or 2.87%.

From Fig. 21, where a vorticity snapshot is presented, it can be seen that qualitatively the structure of the wake remains unchanged from the optimal sinusoidal control forced case to the optimal periodic forced case. This suggests that the effects of the higher frequencies are only felt close to the boundary, but do not significantly affect the wake. The time evolution of the drag and its pressure and viscosity contributions are shown in Fig. 22. We observe that the reduction in the pressure drag is slightly higher than the reduction in the viscous drag. In Fig. 23, a time-averaged profile of the viscous drag contribution over the cylinder surface is shown, in comparison with the unforced and optimal sinusoidal forced cases. The reduction in the viscous drag occurs mainly at the peaks of the profile, namely at $\theta = 60$ and $\theta = 300$.

At $\mathrm{Re} = 1000$, we have, from a qualitative point of view, the same behavior as at $\mathrm{Re} = 200$, as shown in Figs. 24–27. Compared to the optimal sinusoidal control, the optimal control brings an additional drag reduction of no more than 2%, suggesting that engineering intuition was right when suggesting drag reduction via sinusoidal control.

9. CONCLUSIONS

Through a parametric search in forcing amplitude and frequency, minima were found for the drag reduction coefficient for flow around a spinning cylinder at Reynolds numbers 200 and 1000. These minima corresponded to drag reductions of 31% at Reynolds number 200 and 61% at Reynolds number 1000. These results are qualitatively consistent with the

experimental drag reduction of 80% at Reynolds number 15,000 found by Tokumaru and Dimotakis [36]. This suggests the potential for significant drag reduction effects, increasing with Reynolds number, at least up to the critical Reynolds number of 300,000.

Under conditions of optimal forcing, it was noted that the wakes were smaller, were less energetic, and had smaller spreading angles compared with the unforced case. Also, to generate the flow field necessary for maximum drag reduction, increased amplitude of forcing was required as the oscillation frequencies increased. The quasi-optimal forcing conditions determined by parametric search agreed closely with those found by application of optimal control theory. The theory predicted, and it was confirmed by simulation, that further drag reduction could be achieved by adding higher harmonics to the forcing oscillations. This was achieved by extending the time interval of minimum drag at the expense of slightly higher, narrower peaks of maximum drag; however, the improvement is fairly small.

While drag reduction through oscillatory rotation provides an excellent demonstration of the application of optimal forcing control theory, it is clearly of little practical significance. In that direction the use of low-order models (based for example on *proper orthogonal decomposition* (POD)) may lead to control techniques less computationally demanding than the one discussed in the present paper (these methods are discussed in detail in [14, 15], which also provide further references and point out current limitations of the reduced model approach). However, the application of the theory discussed in this article to other forcing techniques such as variable (in space and time) blowing and suction at the walls could lead to some new forcing strategies for more complex shapes like airfoils. We are currently engaged in such studies, the results of which will be reported in the near future.

ACKNOWLEDGMENTS

The authors thank M. Berggren, M. Heinkenschloss, J. L. Lions, T. W. Pan, O. Pironneau, and B. Stoufflet for helpful comments and suggestions. The support of Dassault Aviation and of the Higher Education Texas Coordinating Board is also acknowledged.

REFERENCES

1. H. M. Badr, M. Coutanceau, S. C. R. Dennis, and C. Ménard, Unsteady flow past a rotating circular cylinder at Reynolds numbers 10^3 and 10^4, *J. Fluid Mech.* **220**, 459 (1990).
2. H. M. Badr, S. C. R. Dennis, and P. J. S. Young, Steady and unsteady flow past a rotating circular cylinder at low Reynolds numbers, *Computers and Fluids* **17**(4), 579 (1989).
3. D. Barkley and R. D. Henderson, Three-dimensional Floquet stability analysis of the wake of a circular cylinder, *J. Fluid Mech.* **322**, 215 (1996).
4. M. Berggren, Numerical solution of a flow-control problem: Vorticity reduction by dynamic boundary action. *SIAM J. Sci. Comput.* **19**, 829 (1998).
5. M. Braza, P. Chassaing, and H. H. Minh, Numerical study and physical analysis of the pressure and velocity fields in the near wake of a circular cylinder, *J. Fluid Mech.* **165**, 79 (1986).
6. F. Brezzi and M. Fortin, *Mixed and Hybrid Finite Elements Methods* (Springer–Verlag, New York 1991).
7. D. M. Buschnell and J. N. Hefner, *Viscous Drag Reduction in Boundary Layers* (American Institute of Aeronautics and Astronautics, Washington, DC, 1990).
8. M. Chevalier, Drag Reduction for Flow Past a Circular Cylinder using Blowing and Suction. Research Report UH/MD 312, Department of Mathematics, University of Houston (1999).
9. B. Fornberg, A numerical study of steady viscous flow past a circular cylinder, *J. Fluid Mech.* **98**, 819 (1980).

10. O. Ghattas and J.-H. Bark, Optimal control of two- and three-dimensional incompressible Navier–Stokes flows, *J. Comput. Phys.* **136**(2), 231 (1997).
11. V. Girault and P. A. Raviart, *Finite Element Methods for Navier–Stokes Equations: Theory and Algorithms* (Springer–Verlag, New York 1986).
12. R. Glowinski and J. L. Lions, Exact and approximate controllability for Distributed parameter systems, I, in *Acta Numerica 1994*, edited by Arieh Iserles (Cambridge Univ. Press, Cambridge, UK, 1994), p. 269.
13. R. Glowinski and J. L., Lions, Exact and approximate controllability for distributed parameter systems, II, in *Acta Numerica 1995*, edited by Arieh Iserles (Cambridge Univ. Press, Cambridge, UK, 1995), p. 159.
14. W. R. Graham, J. Peraire, and K. Y. Tang, Optimal control of vortex shedding using low-order models. I. Open-loop model development, *Int. J. Numer. Meth. Engrg.* **44**(7), 945 (1999).
15. W. R. Graham, J. Peraire, and K. Y. Tang, Optimal control of vortex shedding using low-order models. II. Model-based control, *Int. J. Numer. Meth. Engrg.* **44**(7), 973 (1999).
16. M. Gunzburger, Navier–Stokes equations for incompressible flows: Finite element methods, in *Handbook on Computational Fluid Mechanics* edited by R. Peyret (Academic Press, Boston, 1999), p. 99.
17. M. D. Gunzburger, *Finite Element Method for Viscous Incompressible Flows: A Guide to Theory, Practice, and Algorithms* (Academic Press, Boston, 1989).
18. M. D. Gunzburger (Ed.), *Flow Control*, *IMA Volumes in Mathematics and its Applications*, (Springer–Verlag, New York/Berlin, 1995), Vol. 68.
19. M. Gad El Hak, Flow control, *Appl. Mech. Rev.* **42**, 261 (1989).
20. J. W. He and R. Glowinski, Neumann control of unstable parabolic systems: Numerical approach, *J. Optim. Theory Appl.* **96**, 1 (1998).
21. J. W. He, R. Glowinski, R. Metcalfe, and J. Periaux, A numberical approach to the control and stabilization of advection–diffusion systems: Application to viscous drag reduction, *Int. J. Comp. Fluid Mech.* **11**, 131 (1998).
22. R. D. Henderson, Nonlinear dynamics and patterns in turbulent wake transition, *J. Fluid Mech.* **352**, 65 (1997).
23. L. S. Hou and S. S. Ravindran, Computations of boundary optimal control problems for an electrically conducting fluid, *J. Comput. Phys.* **128**(2), 319 (1996).
24. D. B. Ingham and T. Tang, A numerical investigation into the steady flow past a rotating circular cylinder at low and intermediate Reynolds numbers, *J. Comput. Phys.* **87**, 91 (1990).
25. K. Ito and S. S. Ravindran, A reduced-order method for simulation and control of fluid flows, *J. Comput. Phys.* **143**(2), 403 (1998).
26. G. E. Karniadakis and G. S. Triantafyllou, Frequency selection and asymptotic states in laminar wakes, *J. Fluid Mech.* **199**, 441 (1989).
27. D. C. Liu and J. Nocedal, On the limited memory BFGS method for large optimization, *Math. Prog.* **45**, 503 (1989).
28. A. Nordlander, Active Control and Drag Optimization for Flow Past a Circular Cylinder, Research Report UH/MD 248, Department of Mathematics, University of Houston (1998).
29. O. Pironneau, *Finite Element Method for Fluids* (Wiley, Chichester 1989).
30. L. Prandtl, The Magnus effect and windpowered ships, *Naturwissenschaften* **13**, 93 (1925).
31. W. H. Press, S. A. Teukolsky, W. T. Vetterling, and B. P. Flannery, *Numerical Recipes in C: The Art of Scientific Computing*; 2nd ed. (Cambridge University Press, Cambridge, UK/New York, 1994).
32. A. Roshko, On the Development of Turbulent Wakes from Vortex Streets, NACA Rep. 1191 (1954).
33. A. Roshko, On the wake and drag of bluff bodies, *J. Aerosp. Sci.* **22**, 124 (1955).
34. S. S. Sritharan (Ed.), *Optimal Control of Viscous Flows* (SIAM. Philadelphia, 1998).
35. M. Tabata and K. Itakura, A precise computation of drag coefficients of a sphere, *Int. J. Comp. Fluid Dyn.* **9**, 303 (1998).
36. P. T. Tokumaru and P. E. Dimotakis, Rotary oscillation control of a cylinder wake, *J. Fluid Mech.* **224**, 77 (1991).
37. C. H. K. Williamson, Oblique and parallel modes of vortex shedding in the wake of a circular cylinder at low Reynolds numbers, *J. Fluid Mech.* **206**, 579 (1989).